ACS OMEGA

Open Access

http://pubs.acs.org/journal/acsodf

Article

Study of Kinetics and the Working Mechanism of Silica-Coated Amino-Functionalized $CoFe_2O_4$ Ferrite Nanoparticles to Treat Wastewater for Heavy Metals

Muhammad Umer Saleem, Humaira Hussain, Shazia Shukrullah,* Muhammad Yasin Naz,* Muhammad Irfan, Saifur Rahman, and Abdulnoor Ali Jazem Ghanim

Cite This: *ACS Omega* 2024, 9, 3507−3524

Read Online

ACCESS | Metrics & More | Article Recommendations

ABSTRACT: This study used a simple coprecipitation method to produce pristine, silica-coated, and amino-functionalized $CoFe_2O_4$ nanoadsorbents. Amino-functionalization was done to increase the active surface area and metal ion removal efficiency. Both pristine and functionalized adsorbents were employed to recover Pb(II), Zn(II), and Cu(II) ions from wastewater. The adsorption tests were performed by varying the initial concentration of metal ions and contact time at a fixed pH of 6.5. Atomic adsorption spectroscopy was utilized to detect the proportion of metals removed from water. Additionally, the pseudo-first-order, pseudo-second-order, Freundlich, and Langmuir models were employed to compute the kinetic and isothermic data from metal ion adsorption onto the adsorbents. The amino-functionalized adsorbent showed adsorption capacities of 277.008, 254.453, and 258.398 mg/g for Cu(II), Pb(II), and Zn(II) ions, respectively. According to the adsorption results, the Langmuir isotherm and the pseudo-second-order model best suit the data. The best fitting of the pseudo-second-order model with the data indicates that coordinative interactions between amino groups and metal ions are responsible for chemisorption. The metal ions bind with $-NH_2$ groups on the adsorbent surface through chelate bonds. Chelate bonds are extremely strong and stable, indicating the effectiveness of the $CoFe_2O_4@SiO_2-NH_2$ adsorbent in adsorbing heavy-metal ions. The tested adsorbent exhibited good performance, batter stability, and good reusable values around 77, 81, and 76% for Cu(II), Pb(II), and Zn(II) ions, respectively, after five adsorption cycles.

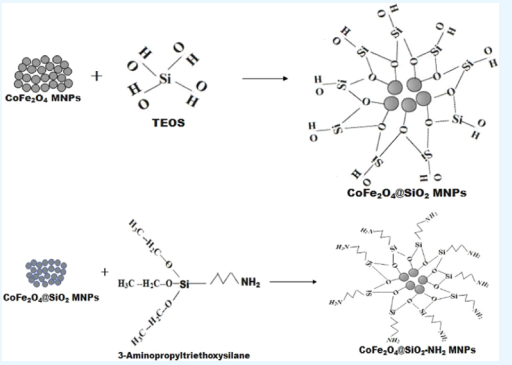

INTRODUCTION

Increased water contamination from industrial pollutants, agricultural operations, and urban residential waste seriously threatens global water quality.[1] Human activities such as industrial production, mining, and using these metals in various products have significantly enhanced the discharge of these metals into our environment. Ions of metals such as lead, arsenic, cadmium, copper, zinc, mercury, and radionuclides such as $^{235}U(VI)$, $^{90}Sr(II)$, and other persistent actinides exhibit exceptionally high toxicity, radioactivity, radiotoxicity, and mobility in ecological systems.[2] The major causes of Zn(II), Cu(II), and Pb(II) pollution are mining and ore processing industries.[3] These metals enter into our environment when used in industrial operations, including metal smelting, plating, and battery manufacturing.[4] These metals can be found in industrial waste in substantial amounts and can subsequently find their way into the land, water, and air. Water contaminated with these metals can seriously impact human and aquatic life. These heavy metals are toxic and cause many health issues, depending on the level of exposure.[5] The exposure to contaminated water can lead to gastrointestinal issues including nausea, vomiting, and diarrhea. Long-term exposure can lead to more serious health problems like kidney and liver damage, anemia, and neurological damage.[6] Pregnant women and babies are more vulnerable to exposure to heavy metals.[7] These metals can accumulate in fish and other aquatic organisms, leading to deformities, reproductive issues, and even death.[8,9]

To avoid these detrimental situations, heavy-metal ion content in water sources must be reduced by improving waste management practices, increasing regulation of industrial activities, and using filtration systems for the treatment of drinking water.[10] Due to distinct physical and chemical traits, metal nanoparticles have demonstrated the potential of

Received: September 19, 2023
Revised: December 22, 2023
Accepted: December 28, 2023
Published: January 10, 2024

Scheme 1. Illustration of Silica Coating and Amino-Functionalized $CoFe_2O_4$ Nanoparticles

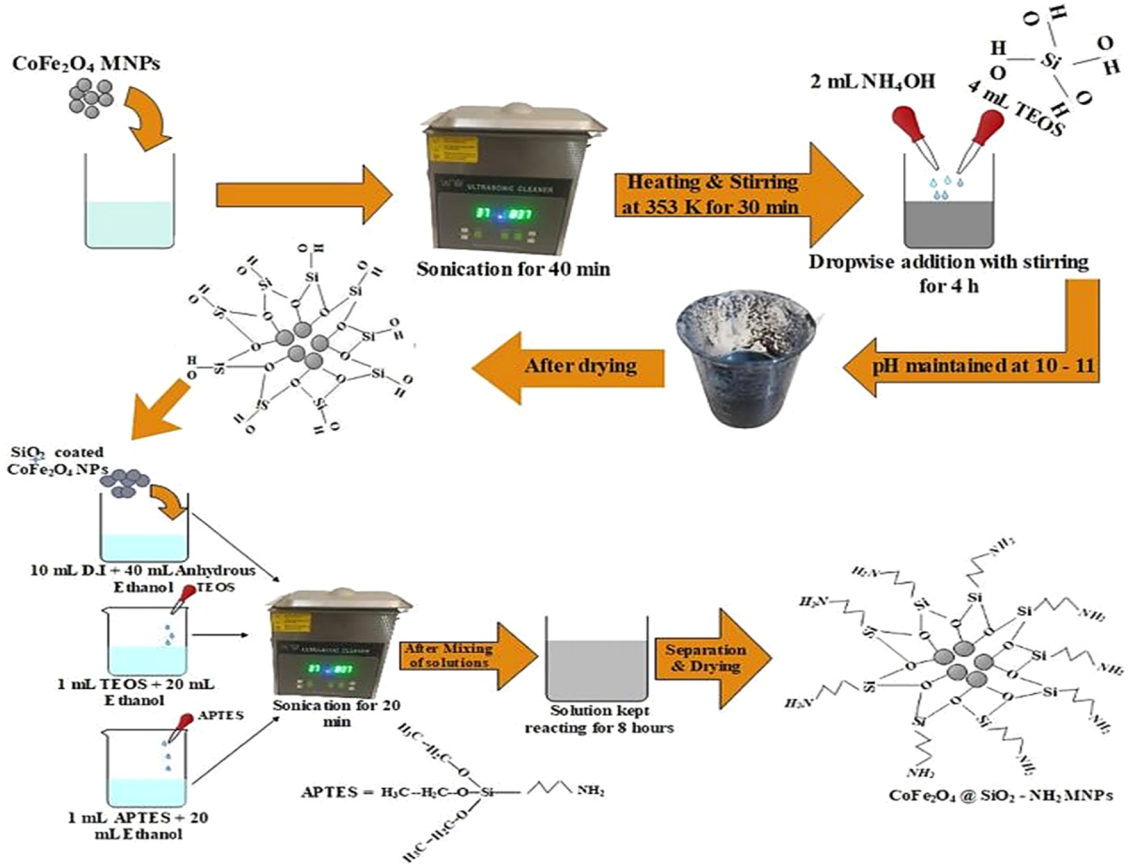

removing heavy metals from wastewater.[11] Researchers have been working for years to find novel approaches to remove heavy metals from water by employing magnetic composite materials. Yao et al.[12] worked on organic contaminants, colloids, and tiny particles, which are challenging to separate using traditional techniques. They revealed that these particles can be separated through magnetic nanoparticle-based adsorbents. Magnetic adsorbents can simultaneously collect multiple heavy metals, including chromium, lead, cadmium, zinc, copper, etc. Because they are so simple to separate after use, magnetic absorbent materials are increasingly in demand to eliminate contaminants. The magnetic nanoparticles provide good magnetic characteristics to adsorbents, allowing them to be separated from the treated solution using a strong magnet bar or an external magnetic field. The magnetic characteristics streamline the adsorption and recovery of adsorbent and make wastewater treatment an economical and effective process. The large surface area of silica-treated and amino-functionalized $CoFe_2O_4$ provides a high number of active sites for the adsorption of metal ions. They are very reactive and efficient at binding to heavy-metal ions in water because of their small size and high surface-area-to-volume ratio.[13] Iron oxide,[14] titanium dioxide,[15] carbon-based nanoparticles,[16] and chitosan-based[17] nanoparticles are also being tested for wastewater treatment.[18,19] These adsorbents are modified with functional groups targeting heavy-metal ions, making them highly selective in binding.[20,21]

In the present research, $CoFe_2O_4$ is preferred over other magnetic nanoparticles to treat wastewater for heavy metals. Due to the high magnetic susceptibility, the applied magnetic field can strongly attract these nanoparticles. $CoFe_2O_4$ nanoparticles also exhibit high corrosive and chemical stability. This material exhibits moderate magnetic coercivity, remanent magnetization, and saturation magnetization.[22] $CoFe_2O_4$ nanoparticles also show stable behavior over various temperatures and are biocompatible, making them safe for water treatment applications.[23] However, pristine $CoFe_2O_4$ nanoparticles dissolve quickly in acidic media and form large aggregates with fewer reactive groups. Because of better stability in acidic environments, silica coating shields the magnetite core from dissolution.[24] The modification of the surface of $CoFe_2O_4$ nanoparticles can be achieved through functionalization with organic or inorganic compounds, which can introduce surface charge, hydrophobicity, or specific functional groups that can interact with the ions of heavy metals. The surface modification also improves the stability and dispersibility of the nanoparticles in the water, preventing agglomeration and enhancing their performance in wastewater treatment.[25−30] This work aims to investigate a facile, environmentally friendly, and easy approach for developing $CoFe_2O_4$ adsorbents using amino as the grafted group to increase their adsorption capacity.

MATERIALS AND METHODS

Chemicals. 3-Aminopropyltriethoxysilane (APTES, $C_9H_{23}NO_3Si$, 99%) and tetraethyl ortho silicate (TEOS, $C_8H_{20}O_4Si$, 98%) were bought from Macklin Reagent (Shanghai, China). Iron(III) nitrate nanohydrate, cobalt nitrate hexahydrate, sodium hydroxide (NaOH), ammonia–water (NH_4OH), lead(II) nitrate, zinc acetate, copper(II) nitrate trihydrate, and ethanol were supplied by Merck. All of

https://doi.org/10.1021/acsomega.3c07200
ACS Omega 2024, 9, 3507−3524

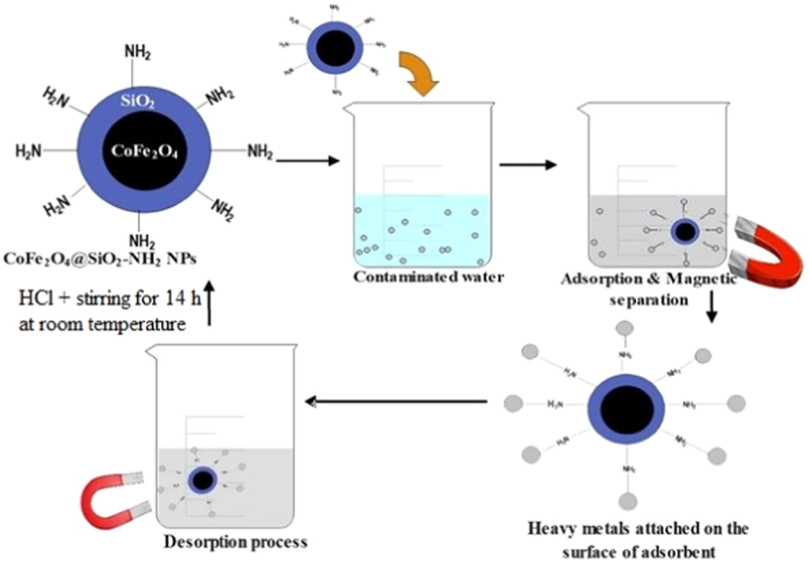

Figure 1. Illustration of the adsorption and desorption processes of functionalized nanoparticles.

the chemicals utilized in this investigation were of analytical reagent grade.

Preparation of the $CoFe_2O_4$ Adsorbent. The coprecipitation technique was used to create cobalt ferrite nanoparticles.[31] Iron nitrate and cobalt nitrate were used in a 2:1 molar ratio. For this, 100 mL of deionized water was mixed with 12 g of iron nitrate and 5 g of cobalt nitrate, and the mixture was stirred for 30 min. Subsequently, NaOH solution was introduced dropwise while maintaining continuous agitation until the pH reached 10. The resulting solution was then agitated for 2 h. The obtained brownish precipitates were then centrifuged with water and ethanol. Precipitates were dried at 100 °C for 24 h before being subjected to 4 h of calcination at 800 °C to produce magnetic adsorbent nanoparticles.

Silica Coating of the $CoFe_2O_4$ Adsorbent. $CoFe_2O_4$ adsorbent nanoparticles were coated with silica (SiO_2) by following the work of Ren et al.[22] Briefly, 2 g of $CoFe_2O_4$ nanoparticles were dispersed in distilled water and subjected to sonication for 40 min. The resultant magnetic solution was then heated at 353 K and agitated for an additional 30 min. Then, silica coating was done at 353 K for 3 h by adding 4 mL of TEOS and 2 mL of NH_4OH to maintain the pH of the solution around 10−11. The solution was then dried at 333 K, rinsed with purified water, and magnetically separated. Scheme 1 depicts the mechanism of the silica coating on nanoparticles.

Amino-Functionalization of the $CoFe_2O_4$@SiO_2 Adsorbent. For amino-functionalization, 10 mL of distilled water and 40 mL of anhydrous ethanol were initially mixed with 1 g of silica-coated adsorbent and ultrasonically dispersed. Another solution was made with 1 mL of TEOS in 20 mL of ethanol. The mixture was mixed with the already-prepared solution and stirred for 10 min after being subjected to sonication for 20 min. Additionally, 1 mL of APTES was separately sonicated with 20 mL of ethanol and subsequently added to the solution. The solution then kept reacting for 8 h. During the reaction, amino groups attach to the $CoFe_2O_4$@SiO_2 surface through the interaction of Si−OH with $-CH_3$ in APTES. Finally, the prepared $CoFe_2O_4$@SiO_2−NH_2 was washed until the pH reached a neutral level. The final product was subjected to a drying process and stored for adsorption application. The steps of preparation of the amino-functionalized adsorbent are shown in Scheme 1.

The silica coating of $CoFe_2O_4$ nanoparticles modifies their surface through the addition of certain functional groups that improve particle stability.[32] Through siloxane linkages, silica forms a covalent bond with the surface of $CoFe_2O_4$. The formation of these bonds occurs via a reaction between the hydroxyl groups on the surface of $CoFe_2O_4$ and the silanol groups. The TEOS creates Si−OH, which then combines with Fe−OH on the nanoparticle surface. This reaction results in the production of $CoFe_2O_4$, predominantly covered within a silica shell. The Si−OH groups of $CoFe_2O_4$@SiO_2 engaged in a reaction with $-CH_3$ derived from APTES. The Fourier transform infrared (FTIR) analysis of the composite material confirmed that this reaction adds amino groups on its surface.

Adsorption of Heavy Metals. To gain insight into the adsorption of metal ions by the adsorbent, the agitation time and initial concentration of metal ions were changed. Studies were conducted by dissolving 0.045 g/L concentration of lead nitrate ($Pb(NO_3)_2$), zinc acetate ($ZnC_2H_3O_2)_2$, and copper nitrate ($Cu(NO_3)_2$) in water. Then, 70 mg of the prepared pristine nanoparticles were introduced to 200 mL of wastewater in a beaker. Samples were taken at specified periods during 500 min of stirring with a pH of 6.5. To test the impact of the amino coating on the adsorption process, the same method was carried out again, utilizing functionalized nanoparticles. The adsorption isotherms were investigated at pH 6.5 and room temperature with solutions of $Cu(NO_3)_2$, $(ZnC_2H_3O_2)_2$, and $Pb(NO_3)_2$, having initial concentrations in the range of 0.025−0.35 g/L. The solution was stirred for mixing and adsorption of metal ions. Atomic absorption spectroscopy was employed to quantify the residual ions in the supernatant after removal of the adsorbent from the solution. Figure 1 illustrates the adsorption and desorption process. Adsorption creates a layer of metallic ions, or adsorbates, on the surface of adsorbents. Since adsorption is a reversible process under some conditions, it may be replicated for several cycles using a desorption technique. The following primary steps are involved in the adsorption of metal ions on the surface of the adsorbent: the pollutant is transported from the polluted solution to the surface of the adsorbent, adsorption

https://doi.org/10.1021/acsomega.3c07200
ACS Omega 2024, 9, 3507−3524

occurs on the solid substrate, and the pollutant is transported within the adsorbent particle. Charged metallic ions of Cu(II), Pb(II), and Zn(II) adsorb on differentially charged amino-functionalized adsorbents due to electrostatic attraction. The metallic substances have a strong affinity for surfaces containing hydroxyl (−OH) or other functional groups.

After the adsorption process, 0.3 g of each adsorbent was washed with 100 mL of 0.2 M HCl for the desorption of Cu, Zn, and Pb heavy metals. For this purpose, the mixture was stirred at 200 rpm using a stirrer for 14 h. Subsequently, the amount of metal ions in the solution was determined. The adsorbent was magnetically separated, washed, and dried for the next cycle. Each adsorbent sample was used for five cycles to check its stability and reusability.

Measurements and Characterizations. X-ray diffraction spectra were generated using a Bruker D6 spectrometer to study the phase structures of pristine, silica-coated, and amino-functionalized adsorbents. The diffraction data were acquired throughout the 2θ range of 20−80° with a step size of 0.02°. The UV−visible analysis was conducted in the 200−800 nm range using a Cecil CE-7200 spectrometer. This analysis was used to study the optical band gap of the adsorbent. The FTIR spectra of the adsorbents were produced in 4000 to 500 cm^{-1} range using a Cary-630 FTIR spectrophotometer. The spectra were analyzed to study the bond formation and functional groups of the adsorbents. A scanning electron microscopy (SEM) Nova-Nano 450 SEM instrument was employed to investigate the surface morphology of the adsorbents. Using a vibrating-sample magnetometer (VSM, 7407), the magnetization values of the adsorbents were measured as a function of the applied magnetic field at room temperature. Metal ion concentrations were determined using an Atomic Absorption Spectrophotometer (Hitachi Polarized Zeeman AAS, Z-8200 Japan).

RESULTS AND DISCUSSION

FTIR Analysis of Adsorbents. The functionalized and pristine adsorbent samples were analyzed for functional groups. FTIR spectra were produced to determine the various groups present in the samples. The composition and surface functional groups were analyzed in Figure 2. A minor peak in the

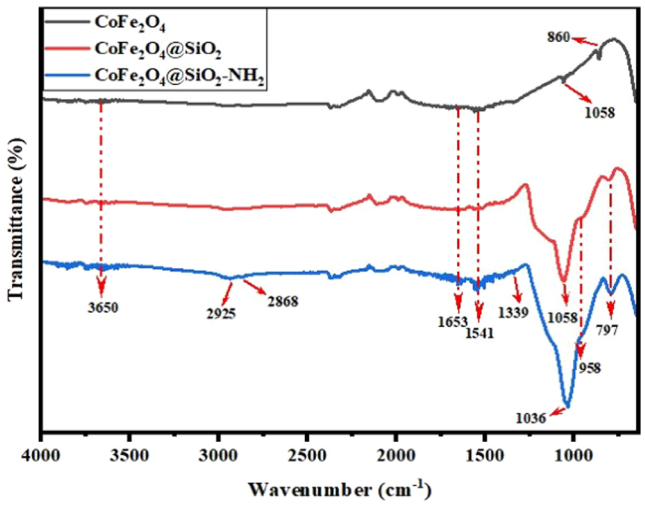

Figure 2. FTIR spectra of pristine, silica-coated, and amino-functionalized adsorbents.

$CoFe_2O_4$ spectrum was found at 860 cm^{-1}, as suggested by Ren et al.[22] This peak was caused by the particular spinel crystal structure of nanoparticles, which is assigned to vibrational mode surface Co−O bonds. The Co−O bond is quite strong; therefore, it does not vibrate as much as other bonds in the structure. Some peaks were suppressed in the silica- and amino-modified nanoparticles due to the presence of silica on the nanoparticle and the reaction between the amino group and the surface Co−O bonds, which caused alterations in their vibrational properties. As proposed by Wang et al.[33] and Lan et al.,[34] a peak at 797 cm^{-1} in the spectrum of silica-modified nanoparticles is ascribed to the symmetrical stretching vibration of Si−O−Si bond in silica coating. In the amino-coated adsorbent, the peak became more intense due to the formation of a hydrogen bond with the silica coating.

The Si−OH stretching vibration confirms the existence of a silica coating on the particle surface. A minor spectral band at around 958 cm^{-1} is consistent with the findings of Wang et al.[33] Additionally, peaks at 1058 and 1036 cm^{-1} are seen in silica-coated and amino-functionalized silica-coated $CoFe_2O_4$ samples, which is consistent with the conclusions made by Lan et al.[34] These peaks are assigned to asymmetrical stretching vibration of Si−O−Si bond and the stretching mode of C−O bond in the amino coating, respectively. A peak at 1058 cm^{-1} was seen in the spectra, which is caused by the metal−oxygen (M−O) bond stretching mode in the $CoFe_2O_4$ nanoparticles. A peak observed at 1339 cm^{-1} is assigned to the deformation vibration of the −NH group, indicating the existence of an amino group. Furthermore, a peak at 1541 cm^{-1} in the spectra of $CoFe_2O_4$ and silica-coated $CoFe_2O_4$ is assigned to the asymmetric stretching vibration of the carboxylate group, confirming the presence of COO^- in all peaks. However, the peak observed at the same wavelength in the spectra of $-NH_2$-functionalized silica-coated $CoFe_2O_4$ is more intense, possibly due to the carboxylate group attachment to the functionalized adsorbent. Finally, a peak at 1653 cm^{-1} is attributed to H−OH vibration bending of the absorbed water molecules.[33] Peaks at 2868 and 2915 cm^{-1} in the spectra of the $-NH_2$-functionalized silica-coated adsorbent are consistent with the conclusions of Ren et al.[22] These peaks are induced by symmetric stretching vibration and asymmetric stretching vibration of ($-CH_2$) methylene groups present in the alkyl chains of the APTES molecule, which was utilized in amino-functionalization of the adsorbent. In the amino-functionalized adsorbent, an additional peak was seen at 3650 cm^{-1} because of stretching vibrations of silanol (═Si−OH) and physisorbed water (−OH).

Magnetic Properties of Adsorbents. The VSM technique was used to examine the magnetic characteristics of the produced samples. Comparative hysteresis loops are shown in Figure 3. $CoFe_2O_4$ nanoparticles were found to have high M_s, M_r, and H_c values around 75 emu/g, 30 emu/g, and 1379 Oe, respectively, which are analogous to the findings of Zhang et al.[35] and Zalite et al.[36] When the calcination temperature increases, the defect in the material gradually diminishes and the thermal disturbance of atoms at the surface decreases. The regular alignment of the magnetic domains causes an increase in saturation magnetization.[37] In silica-coated adsorbents, the saturation magnetization dropped to 69 emu/g.[38] A reduction in the saturation magnetization indicates that the silica shell was adequately deposited on the surface.

https://doi.org/10.1021/acsomega.3c07200
ACS Omega 2024, 9, 3507−3524

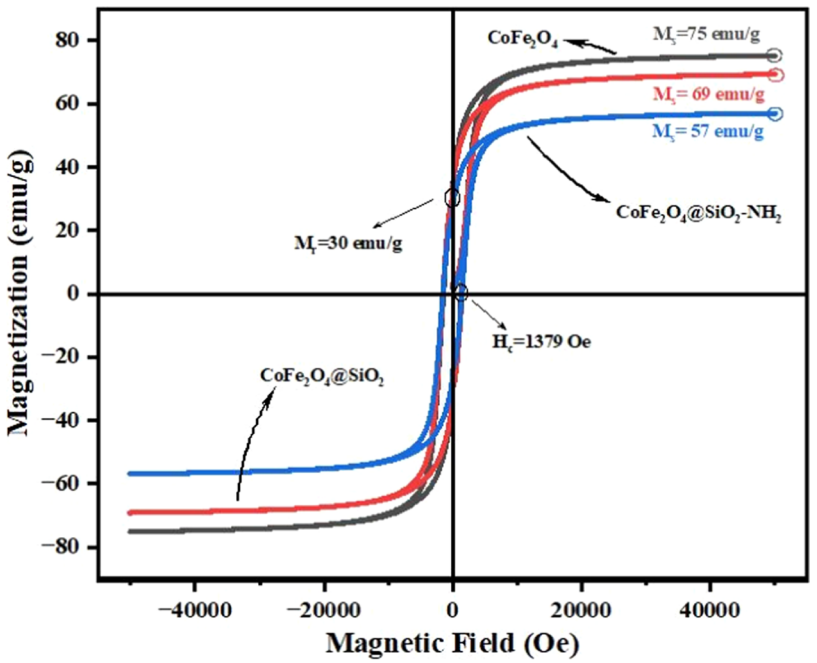

Figure 3. Hysteresis loops of pristine, silica-coated, and amino-functionalized adsorbents.

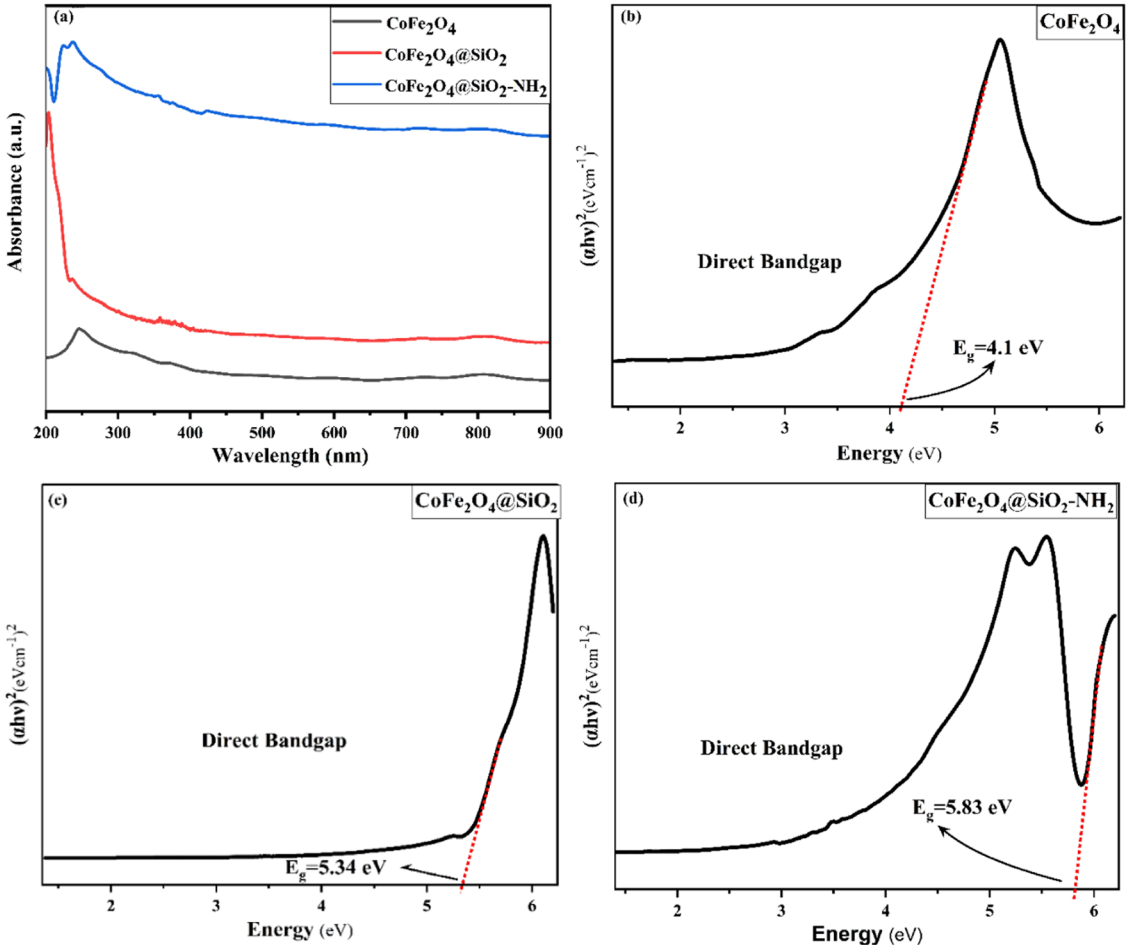

Figure 4. (a) UV spectra of pristine, silica-coated, and amino-functionalized adsorbents, and Tauc plot of (b) pristine, (c) silica-coated, and (d) amino-functionalized adsorbents.

The saturation magnetization for the $-NH_2$-functionalized silica-coated adsorbent decreased further to 57 emu/g due to the amorphous nature of the coating, decreased $CoFe_2O_4$ content in each sample, and an increased layer of organic

https://doi.org/10.1021/acsomega.3c07200
ACS Omega 2024, 9, 3507−3524

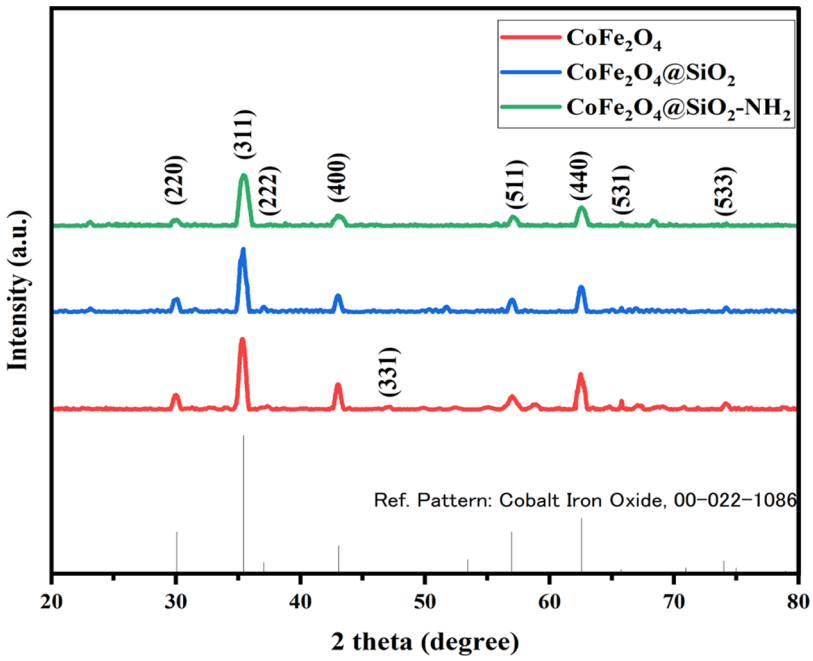

Figure 5. XRD patterns of pristine, silica-coated, and amino-functionalized adsorbents.

Table 1. Structural Parameters Calculated from XRD Data of the Adsorbent

				lattice plane			fwhm				
sr.	2θ (deg)	d-spacing (Å)	d-spacing (Å) JCPDS	h	k	l	β	crystallite size D (nm)	dislocation density $\delta \times 10^{-3}$ (nm^{-2})	microstrain $\varepsilon \times 10^{-3}$	lattice constant (Å)
1	29.98	2.97746	2.9680	2	2	0	0.4401	18.6890	2.8630	7.1692	8.4215
2	35.33	2.53836	2.5310	3	1	1	0.5426	15.3663	4.2351	7.4335	8.4188
3	37.24	2.41196	2.4240	2	2	2	0.5680	14.7588	4.5909	7.3541	8.3553
4	43.01	2.10123	2.0990	4	0	0	0.4365	19.5623	2.6131	4.8336	8.4049
5	47.06	1.92938	1.9260	3	3	1	0.3973	21.8098	2.1023	3.9809	8.4100
6	57.02	1.61383	1.6150	5	1	1	0.7321	12.3490	6.5574	5.8808	8.3857
7	62.52	1.48427	1.4830	4	4	0	0.5675	16.3757	3.7291	4.0787	8.3963
8	65.75	1.41911	1.4190	5	3	1	0.3451	27.4121	1.3308	2.3296	8.3956
9	74.17	1.27738	1.2798	5	3	3	0.3982	25.0076	1.5990	2.2986	8.3763

shell on nanoparticle. The silica-coated amino-functionalized adsorbents showed coercive force and remanent magnetization values comparable to the pristine magnetic adsorbent.[22] Even though the surface coatings reduced the magnetic characteristics, the nanoparticles could still readily be separated from the treated water by using an external magnetic field. The redispersion is faster when the applied magnetic field is withdrawn with a minor tremble. Because of the solid−liquid separation and redispersion, which preserves the magnetic characteristics, the produced adsorbents can effectively be employed for the treatment of heavy metals.

UV Spectroscopy of Adsorbents. UV−vis analysis was performed to analyze the optical behavior of coated and uncoated adsorbent samples. The range of UV−vis spectra was set 200−900 nm in Figure 4. The absorbance spectra in Figure 4a show absorbance in the ultraviolet region, proving the semiconducting nature of the samples. As reported in the study of Akhtar et al.,[39] the absorbance is often influenced by a wide range of variables, including the band gap, particle size, lattice parameters, and surface roughness. The Tauc plot relation "$(\alpha h\nu)^2 = B(h\nu - E_g)^{\gamma}$" was used to obtain the energy band gap values for each sample, where $\gamma = 2$ or 1/2 for direct allowed and indirect allowed transitions between the valence and conduction bands.[40] Figure 4b−d displays $h\upsilon$ vs $(\alpha h\upsilon)^2$ plots of pristine, silica-coated, and amino-functionalized adsorbents, respectively. Pristine adsorbent showed a relatively smaller band gap value of 4.1 eV compared to modified adsorbents.[41] The silica and amino-coated samples showed band gap values of 5.34 and 5.83 eV, respectively. These values agree with a previous study by Erdem et al.[42] on silica-coated nanocomposites. In the case of the pristine adsorbent, the optical band gap was small because of the freer charge carriers on lattice sites due to the higher density of metallic cations. As these charge carriers are free to move, even an incident light beam having small energy will cause the charges to move from valence to the conduction band. In the case of silica coating and $-NH_2$-functionalization,[43] all of the adsorbent samples were suitable to work in the UV region when their optical properties are considered in an environmental treatment application or photocatalysis application.

XRD Analysis of Adsorbents. Figure 5 displays XRD patterns of both pristine and modified adsorbents. Clear intensity peaks are visible in the powder sample at 2θ of 29.99 (220), 35.33 (311), 37.25 (222), 43.01 (400), 47.06 (331), 57.02 (511), 62.52 (440), 65.75 (531), and 74.18° (533). This comparison of the peaks with reference patterns reveals that

https://doi.org/10.1021/acsomega.3c07200
ACS Omega 2024, 9, 3507−3524

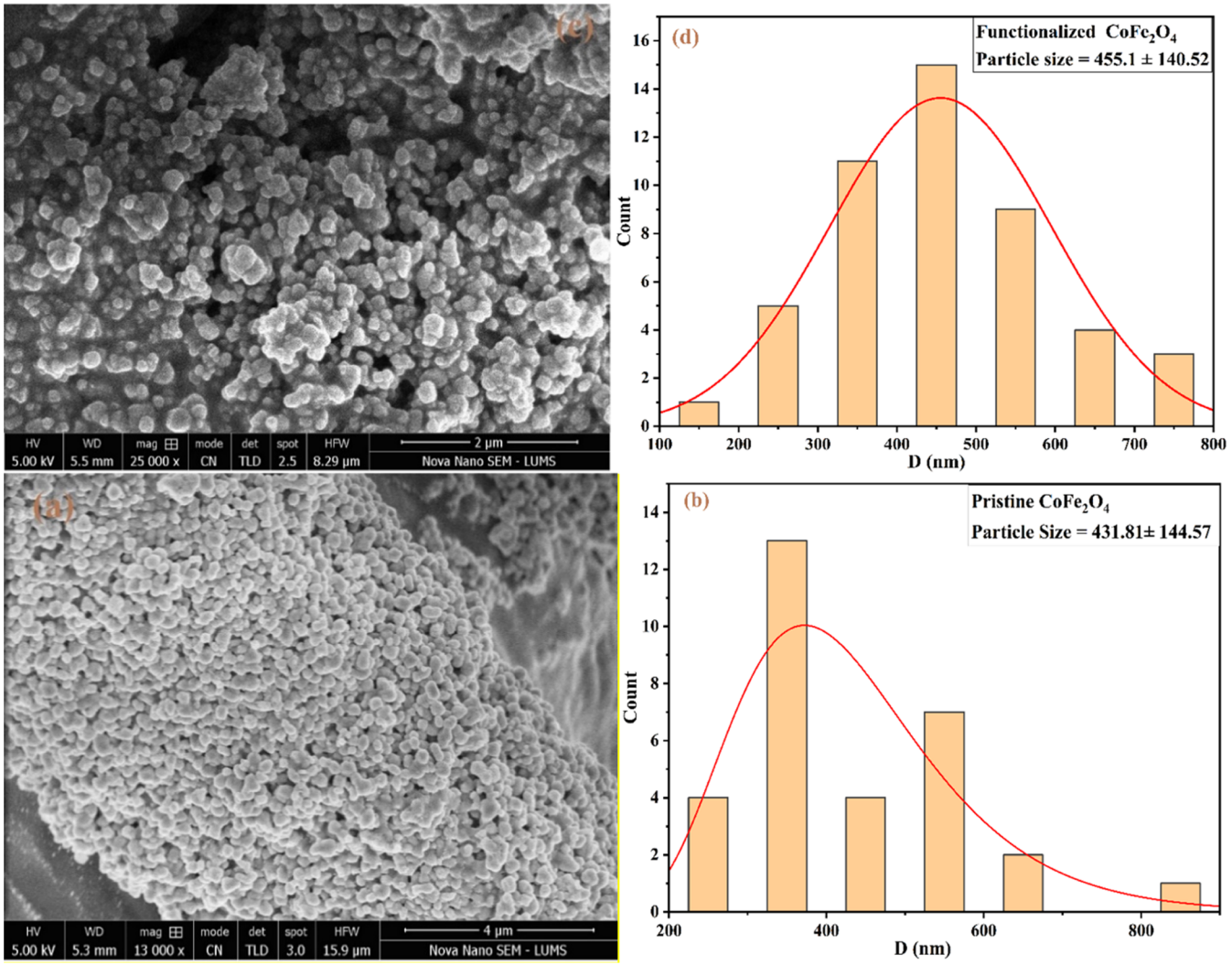

Figure 6. (a) SEM image of the pristine adsorbent, (b) size distribution of the pristine adsorbent, (c) SEM image of the amino-functionalized adsorbent, and (d) size distribution of the amino-functionalized adsorbent.

the prepared samples have a microcrystalline structure. All specific peaks agree with the JCPDS of Cobalt Ferrite (00-022-1086), which verifies the face-centered cubic spinel structure of the adsorbent. Diffraction analysis reveals a fairly strong peak at around 2θ of 35.33°, corresponding to the merging of individual nanostructures.[44] Additionally, the diffraction peaks in silica-coated and amino-functionalized adsorbents are comparable to those of pristine $CoFe_2O_4$, and no additional peaks are noticed aside from a very small peak around 23° in the silica and amino-coated samples, confirming the presence of amorphous silica.[33]

Table 1 lists different XRD-derived parameters such as dislocation density, strain, and lattice constant. Bragg's law in eq 1 was used to relate the diffraction angle with the interplanar distance in the lattice. Lattice constants were determined using the plane spacing in eq 2. The standard value of lattice constant is 8.3919 Å, which was confirmed by the reference JPCDS (card no. 00-022-1086), The experimental value of 8.3960 Å agreed well with the standard value of lattice constant. The Debye−Sherrer formula in eq 3 was employed to obtain the crystallite size of each sample. Here, k is taken as 0.9, β is the full width at half-maximum, θ is Bragg's angle, and λ is the wavelength. These calculations yielded an average crystallite size around 19.0368 nm.[44] The extent of distortion in the crystalline lattice is known as microstrain. It originates from flaws such as stacking faults, triple junctions at grain boundaries, sintering stress, and coherency stress.[43] The microstrain of all of the adsorbent samples is shown in Table 1

$$n\lambda = 2d \sin\theta \tag{1}$$

$$\frac{1}{d^2} = \frac{h^2}{a^2} + \frac{k^2}{b^2} + \frac{l^2}{c^2} \tag{2}$$

$$D = \frac{k\lambda}{\beta \cos\theta} \tag{3}$$

Morphology and Size Distribution of Adsorbents. SEM micrographs were produced to further describe the morphology and size of the pristine and modified adsorbents. Figure 6 compares the surface morphologies of pristine and functionalized adsorbents. SEM images revealed that the average particle size of the unmodified nanoparticles was somewhat smaller than that of the functionalized nanoparticles. The nanoparticles were uniformly shaped and roughly spherical in shape. In modified adsorbents, the salinization and functionalization processes prevented the nanoparticles

https://doi.org/10.1021/acsomega.3c07200
ACS Omega 2024, 9, 3507−3524

from agglomerating due to the magnetic properties, as shown in Figure 6a. However, the pristine sample showed aggregation of the particles due to their strong magnetic characteristics compared to modified nanoparticles, as reported in Figure 6a.[45] The agglomeration of the particles in the pristine sample results in a small reactive surface area compared to the modified sample. In the modified adsorbent, the caping material itself caused some agglomeration among the nanoparticles. The particle size of the pristine nanoparticles was estimated to be 431 nm, as shown in Figure 6b. A small increase in particle size was noticed following the amine-functionalization of the adsorbent, as shown in Figure 6c. After going through amine-functionalization, the particle size was measured at about 455 nm (Figure 6d). This increase in size was due to the deposition of the coating material on the nanoparticles.

■ ADSORPTION OF HEAVY-METAL IONS

Effect of pH on the Adsorption Performance. The pH of the solution plays a significant role in the adsorption process. As the metal hydroxide may precipitate at a pH greater than 7, in previous studies by Wang et al.,[33] experiments were conducted at various pH values between 2 and 10. It was demonstrated that the adsorbents have considerable adsorption toward the ions of heavy metals around a pH value of 7. When the pH of the solution is low, the H^+ ions on the surface of functionalized nanoparticles react with the metal ions, resulting in the protonation of amino groups on the surface. As a result, the rate of heavy-metal adsorption decreases at low pH values.[46,47] According to the study by Zhang et al.,[48] as the pH of the solution increases, H^+ ions begin dissociating from the functional groups until the surface is totally deprotonated, and the competitiveness of H^+ ions weakens as their concentration reduces. The surface becomes negatively charged, enhancing the adsorption capacities of the adsorbent for the said metal ions. Additionally, at low pH, heavy-metal ions and amine group ions ($-NH^{3+}$) show Coulomb repulsions, which also reduces the effectiveness of adsorbents for adsorption.[49] The adsorption properties are based on the presence of amino groups on the surfaces of $CoFe_2O_4$@SiO_2 nanoparticles. As shown in Figure 7, a large number of heavy-metal ions were absorbed when the pH value was close to 7 due to a strong interaction of amino sites on nanoparticles with the metal ions. In a strongly acidic or basic environment, Co ions start to leach from the $CoFe_2O_4$ composition into the solution. The high solubility of Co ions in the solution causes inactivation of the adsorbent. The pH of the solution for the adsorption experiment was adjusted to a neutral level to ensure maximal adsorption of the metal ions.

Effect of Contact Time on the Adsorption Performance. Figure 8 shows the percentage of removal of heavy-metal ions using pristine and functionalized adsorbents with time. All three types of heavy-metal ions showed comparable adsorption. Equation 4 can be utilized to determine the percentage removal of metallic ions after different time intervals. The removal efficiency was significantly high during the first 40−60 min. The adsorption slows down with time and reaches a steady state after 300 min of adsorption time. The adsorption of metal ions by the functionalized adsorbent was notably higher than the pristine adsorbent. The excessive active sites on the functionalized adsorbent compared to the pristine one and the quick dispersal of heavy-metal ions from the contaminated water to the surface of the adsorbent during the initial phases are likely the key causes of the initial rapid rate of removal of metal ions.[50]

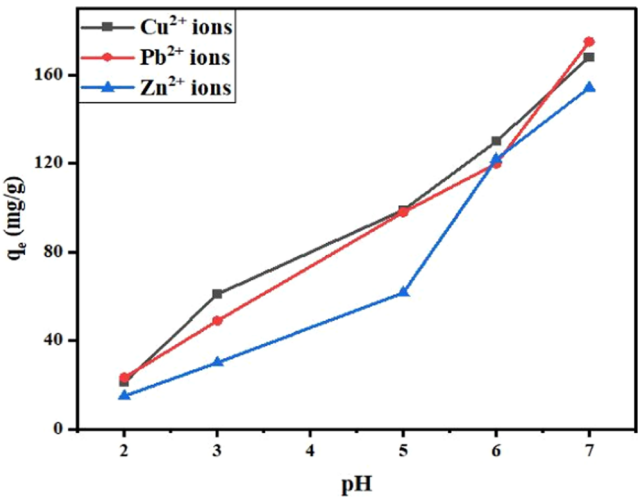

Figure 7. Effect of solution pH on adsorption capacity of the amino-functionalized adsorbent.

The concentration of metal ions reached an equilibrium point after 300 min. Equation 5 can be used to determine the adsorption capacity of the adsorbent. Equation 6 provides the maximum adsorption capacity of the adsorbate

$$\text{removal efficiency}\ (\%) = \frac{C_i - C_f}{C_i} \times 100 \tag{4}$$

$$q_t = \frac{(C_i - C_f)}{m} \times V \tag{5}$$

$$q_e = \frac{(C_i - C_f)}{m} \times V \tag{6}$$

where C_i and C_f represent the initial and final metal ion concentrations in contaminated water. The quantity of the adsorbed metal ions after a specific time is denoted by q_t, while q_e is the maximum adsorption capacity, which represents the amount of metal ions adsorbed per unit mass of the adsorbent at equilibrium; the volume of the contaminated solution is denoted by V, and the mass of the absorbent is denoted by m. The relative adsorption capacities of the adsorbent toward the metal ions over time are shown in Figure 8. The amino-functionalized adsorbent showed roughly 30% higher adsorption capacity than the pristine adsorbent at the end of the process.

Adsorption Kinetics. To comprehend the kinetics of adsorption, two kinetic models were developed known as pseudo-first-order and second-order models. The pseudo-first-order kinetic model is employed for reversible processes when equilibrium is maintained between the solid and liquid phases, suggesting physisorption rather than chemisorption. The pseudo-second-order model clarifies the kinetics of heavy-metal ion adsorption onto adsorbents. The pseudo-first-order model in its linear form is shown in eq 7

$$\frac{dq_t}{dt} = k_1(q_e - q_t) \tag{7}$$

Here, the adsorbate amounts after time "t" and equilibrium are denoted by q_t and q_e (mg/g), respectively. The equilibrium constant of the pseudo-first-order model is denoted by the

https://doi.org/10.1021/acsomega.3c07200
ACS Omega 2024, 9, 3507−3524

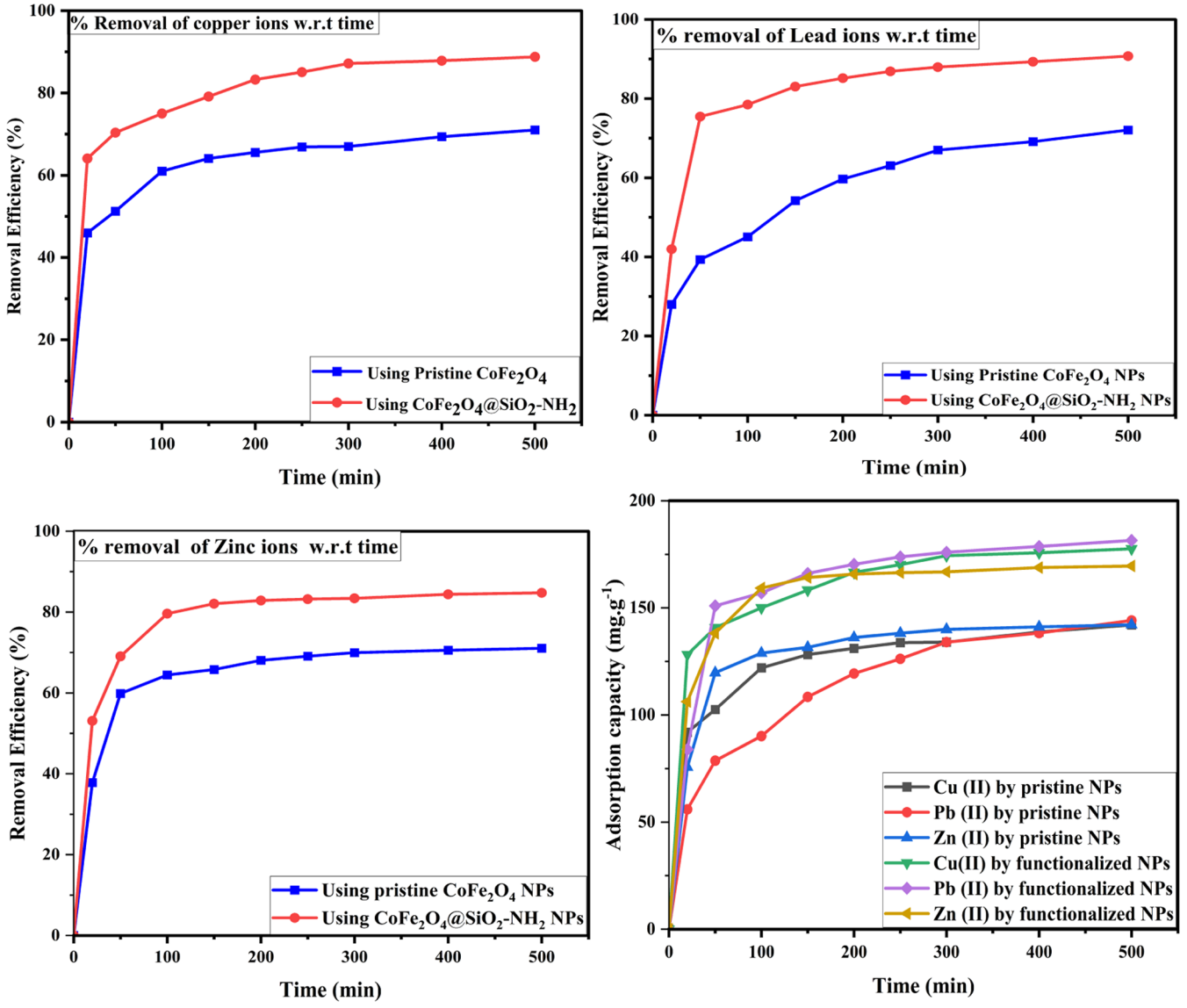

Figure 8. Effect of contact time on the adsorption of metal ions and comparative analysis of the adsorption capacity toward the metal ions.

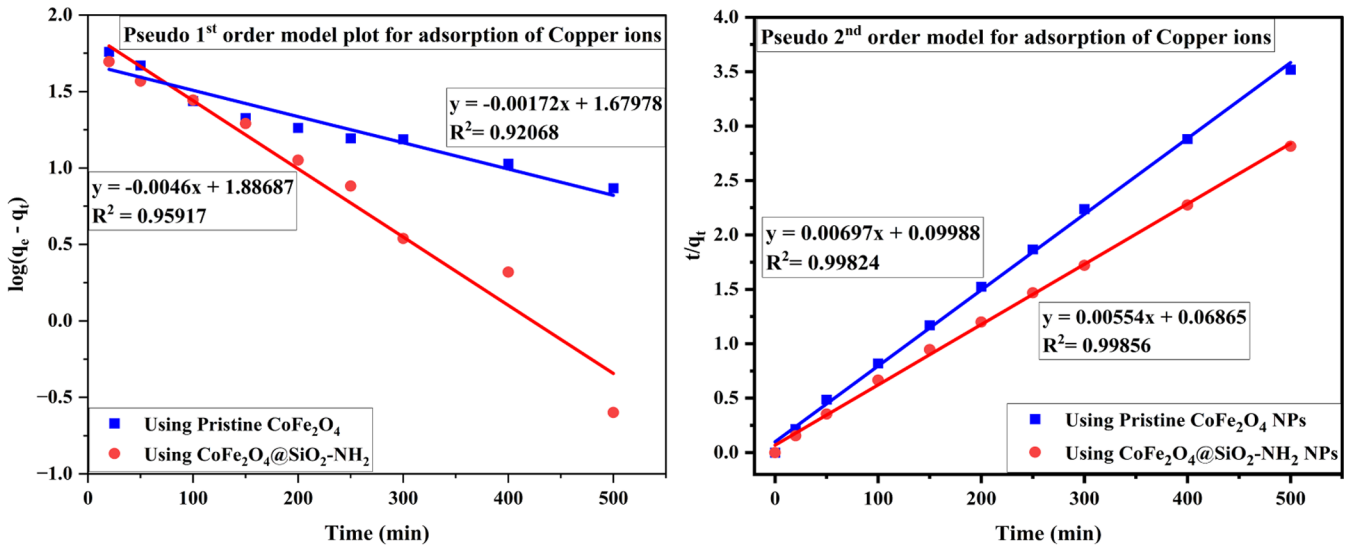

Figure 9. Pseudo-models for the adsorption of Cu(II) ions.

https://doi.org/10.1021/acsomega.3c07200
ACS Omega 2024, 9, 3507−3524

Table 2. Kinetic Parameters for the Adsorption of Cu(II), Pb(II), and Zn(II) Ions

	first-order kinetic model					second-order kinetic model				
	intercept	slope	q_e (mg/g)	k_1	R^2	intercept	slope	q_e (mg/g)	k_2	R^2
				Adsorption of Cu(II) Ions						
pristine $CoFe_2O_4$	1.67978	−0.0017	5.364376	-3.44×10^{-6}	0.92068	0.09988	0.00697	143.472	0.00048639	0.9982
$CoFe_2O_4$@SiO_2-NH_2	1.88687	−0.0046	6.598682	−0.0000092	0.95917	0.06865	0.00554	180.505	0.00044707	0.9986
				Adsorption of Pb(II) Ions						
pristine $CoFe_2O_4$	4.56948	−0.00428	96.49392	−0.00000856	0.9769	0.27332	0.0066	151.5152	0.00015937	0.9868
$CoFe_2O_4$@SiO_2-NH_2	4.35709	−0.00952	78.02974	−0.00001904	0.9293	0.07786	0.0054	185.1852	0.00037452	0.9985
				Adsorption of Zn(II) Ions						
pristine $CoFe_2O_4$	1.5661	−0.00257	4.78794	−0.00000514	0.8644	0.07639	0.00691	144.7178	0.000625057	0.9992
$CoFe_2O_4$@SiO_2-NH_2	1.60305	−0.00403	4.96816	−0.00000806	0.9287	0.04625	0.00581	172.1170	0.000729862	0.9996

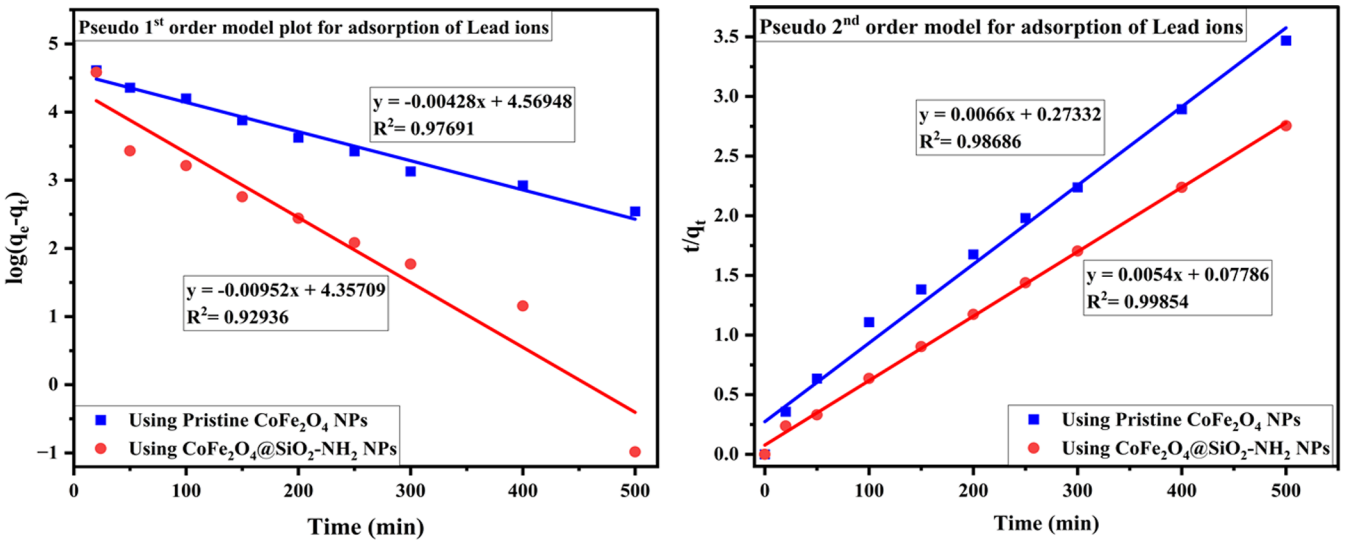

Figure 10. Pseudo-models for the adsorption of Pb(II) ions.

constant k_1. In the pseudo-first-order model, differences between saturation concentration and total amount of solid absorbed over time can be directly related to changes in the rate at which a solute is absorbed. This model is mostly applicable to the early stages of an adsorption process. By integrating and applying limits to the above eq 7, we get eq 8 as

$$\log(q_e - q_t) = \log q_e - \frac{k_1}{2.303}t \tag{8}$$

When studying the relationship between time "t" and $\log(q_e - q_t)$, a plot is produced for the pseudo-first-order model. This linear plot is then compared to the integrated linear form of the pseudo-first-order model. The parameters for the model were obtained using the slope and intercept of the resultant line.[51]

The second-order kinetic model is based on the fact that the adsorption rate is proportional to the number of unoccupied sites and the number of adsorbate molecules in the liquid or gas phase. This model is expressed in the form of eq 9

$$\frac{dq_t}{dt} = k_2(q_e - q_t)^2 \tag{9}$$

It can also be expressed in the form of eq 10 as

$$\frac{1}{q_t} = \frac{1}{k_2 q_e^{\,2}} + \frac{t}{q_e} \tag{10}$$

Also, h can be expressed in the form of eq 11

$$h = k_2 q_e^{\,2} \tag{11}$$

Here, k_2 denotes the rate constant, q_e and q_t are the quantities of adsorbed heavy-metal ions at equilibrium and at time t, respectively, and h indicates the original sorption rate. Plotting q_e versus t/q_t should reveal a specific relation. Using slope $(1/Q_m)$ and intercept, we can calculate the amount of adsorbed adsorbate at equilibrium to obtain the rate constant "k_2".[52] Here, Q_m is the maximum adsorption capacity of the adsorbent.

Pseudo-Models for the Removal of Heavy-Metal Ions. On the basis of pseudo-models, Figure 9 displays a comparison plot of Cu(II) ion adsorption onto synthesized pristine and functionalized adsorbents. According to the work by Vamvakidis et al.,[53] 16.6 mg/g of Cu(II) ions adsorbed on the ferrite nanoparticles under equilibrium conditions. These calculations employed pseudo-first-order kinetics. In our study, the adsorbent showed a maximal adsorption capacity of around 29.1 mg/g at equilibrium. The calculations were based on the utilization of the pseudo-second-order model. The kinetic parameters for the adsorption of Cu(II), Pb(II), and Zn(II) ions are listed in Table 2. The kinetic parameters can be useful in understanding which model is best suited for adsorption data. It is discovered that the second-order model better describes the adsorption of Cu(II) ions on uncoated and functionalized adsorbent. However, the functionalized adsorb-

https://doi.org/10.1021/acsomega.3c07200
ACS Omega 2024, 9, 3507−3524

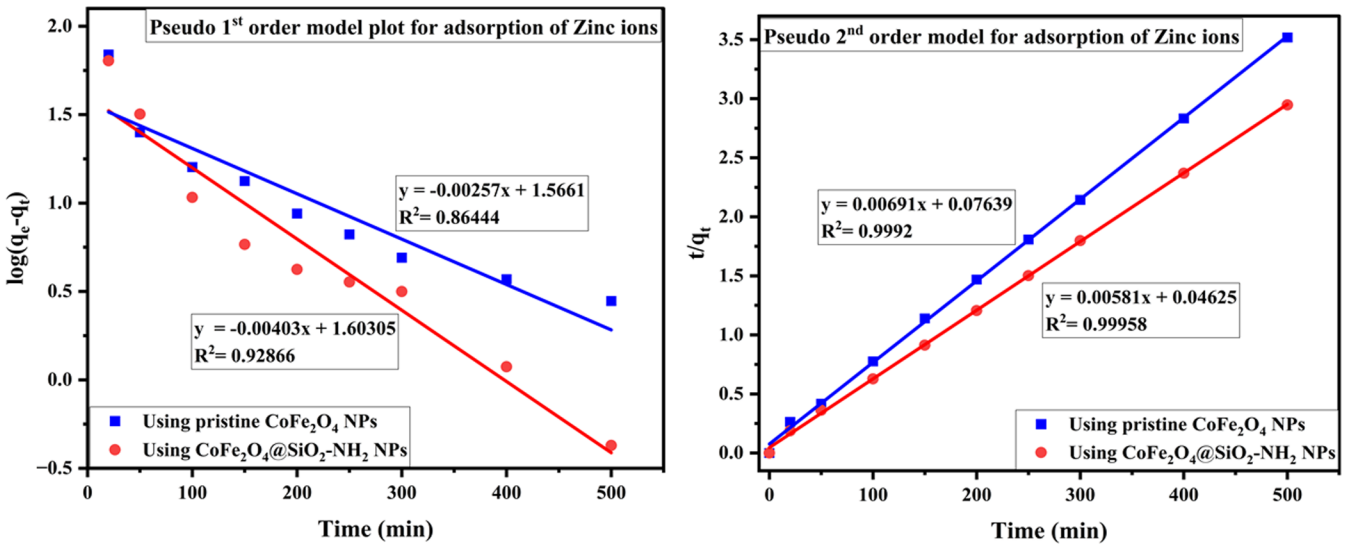

Figure 11. Pseudo-models for the adsorption of Zn(II) ions.

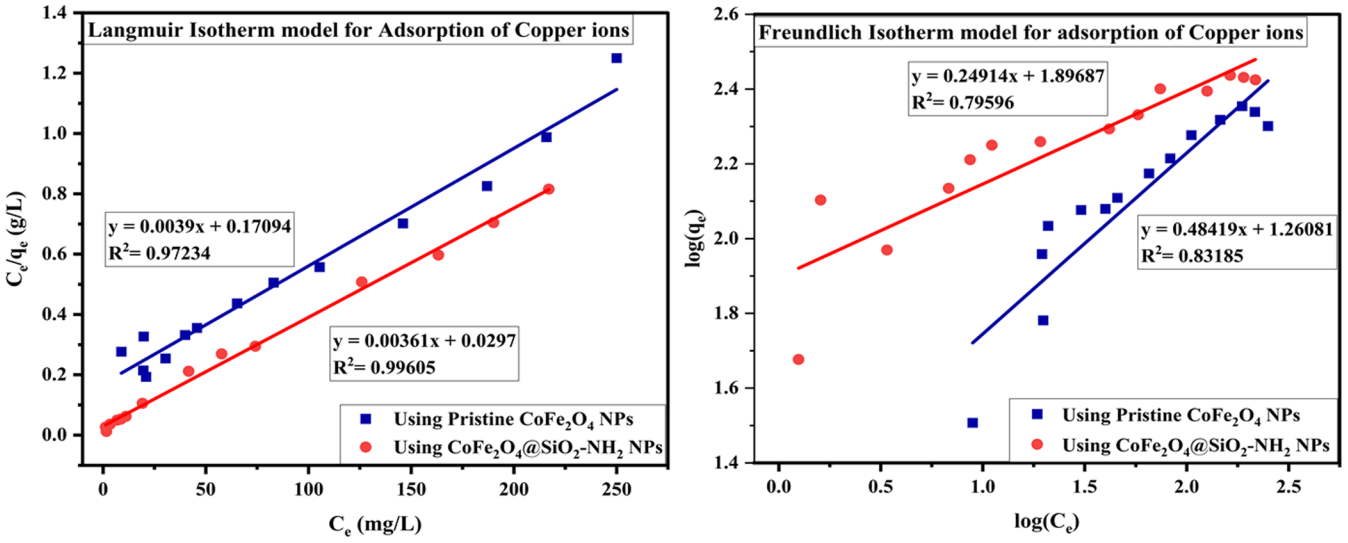

Figure 12. Isotherm models for the adsorption of Cu(II) ions.

ent exhibits higher adsorption capability when compared with the pristine adsorbent, indicating that the amino coating on nanoparticles is effective for applications involving wastewater treatment for heavy metals. The fittings indicate that the pseudo-second-order model best fits the adsorption data, confirming the chemisorption process in the adsorption mechanism of Cu(II) ions according to the previously published work by Sahare et al.[54]

Chemical adsorption, also known as chemisorption, is the process by which adsorbate molecules attach to a solid surface. This happens due to intense chemical interactions between the adsorbate and the surface, such as due to ionic or covalent bonding, creating a monolayer on the surface of the adsorbent with discrete molecule orientations and site specificity. Adsorption frequently includes the exchange of electrons between the surface of the nanoparticles and the adsorbate, forming stable chemical bonds. Chemisorption is distinguished by its energy dependency on surface coverage and temperature, with activation energy often required due to strong intermolecular interactions between the adsorbate and the surface. The pseudo-second-order model generated a straight line that matched the data more correctly than the first-order model, which is in consonant with the results found in the previous investigation of Ren et al.[22] and Vamvakidis et al.[53] The maximal adsorption capacity based on the pseudo-second-order kinetic model is around 180.505 mg g^{-1}, which is much larger than the adsorption capacities obtained using the pristine adsorbent. The results indicate that the method used for Cu(II) ion adsorption on the functionalized adsorbent is chemisorption.

Figure 10 demonstrates the adsorption of Pb(II) ions using pseudo-models. When R^2 was taken into consideration, the pseudo-second-order model produced a straight line that more closely resembled the data than the first-order model, which is in accordance with the conclusions obtained by Baghaei et al.[55] The experimental analysis by Jayalakshmi et al.[23] showed high adsorption of 46.5 and 47.6 mg/g, respectively, for Pb(II) ions onto the magnetic nanoparticles under equilibrium circumstances.

Table 2 displays the parameters calculated from the pseudo-models. The q_e calculated from the experimental data for the functionalized adsorbent is around 78.02 mg g^{-1}, while the

https://doi.org/10.1021/acsomega.3c07200
ACS Omega 2024, 9, 3507−3524

Table 3. Isotherm Parameters for the Adsorption of Cu(II), Pb(II), and Zn(II) Ions

	Langmuir isotherm model					Freundlich isotherm model				
	intercept	slope	q_{max} (mg/g)	K_L	R^2	intercept	slope	n	K_f	R^2
Adsorption of Cu(II) Ions										
pristine $CoFe_2O_4$	0.17094	0.0039	256.410	0.02282	0.97234	1.26081	0.48419	0.48419	3.52828	0.83185
$CoFe_2O_4$@SiO_2-NH_2	0.0297	0.00361	277.008	0.12155	0.99605	1.89687	0.24914	0.24914	6.66500	0.79596
Adsorption of Pb(II) Ions										
pristine $CoFe_2O_4$	0.10747	0.00476	210.084	0.04429	0.93549	1.36685	0.43457	0.43457	3.92298	0.5723
$CoFe_2O_4$@SiO_2-NH_2	0.04881	0.00393	254.453	0.08052	0.9757	1.74059	0.30823	0.30823	5.70071	0.45803
Adsorption of Zn(II) Ions										
pristine $CoFe_2O_4$	0.11063	0.00395	253.165	0.03570	0.95595	1.40351	0.4386	0.4386	4.06946	0.69041
$CoFe_2O_4$@SiO_2-NH_2	0.04256	0.00387	258.398	0.09093	0.98981	1.72798	0.32151	0.32151	5.62927	0.63532

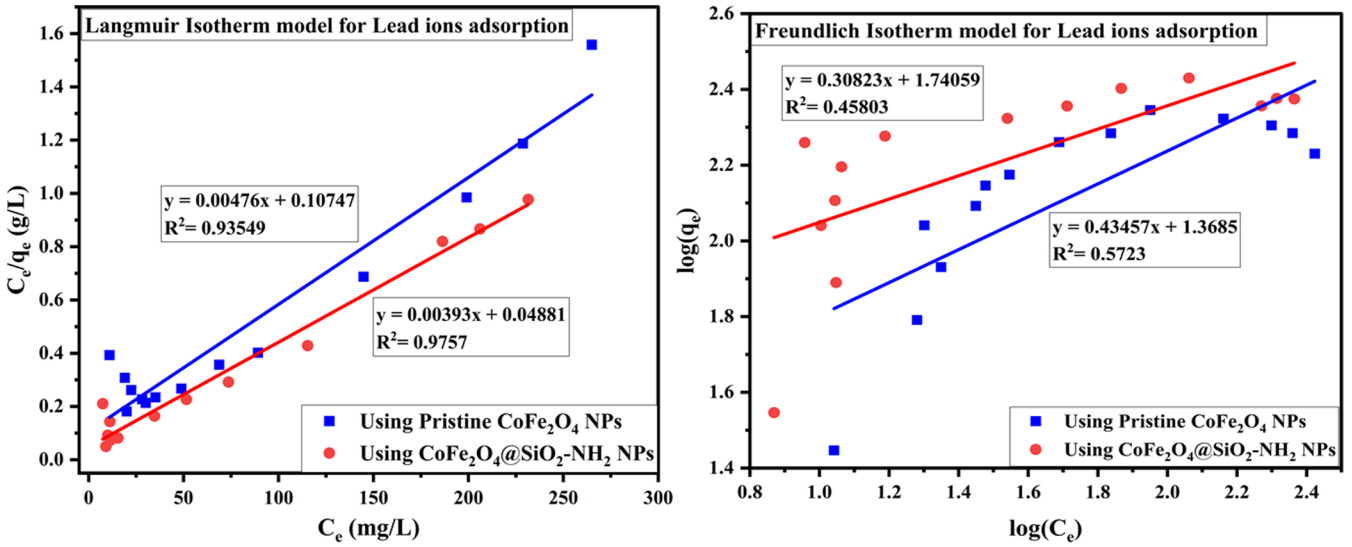

Figure 13. Isotherm models for the adsorption of Pb(II) ions.

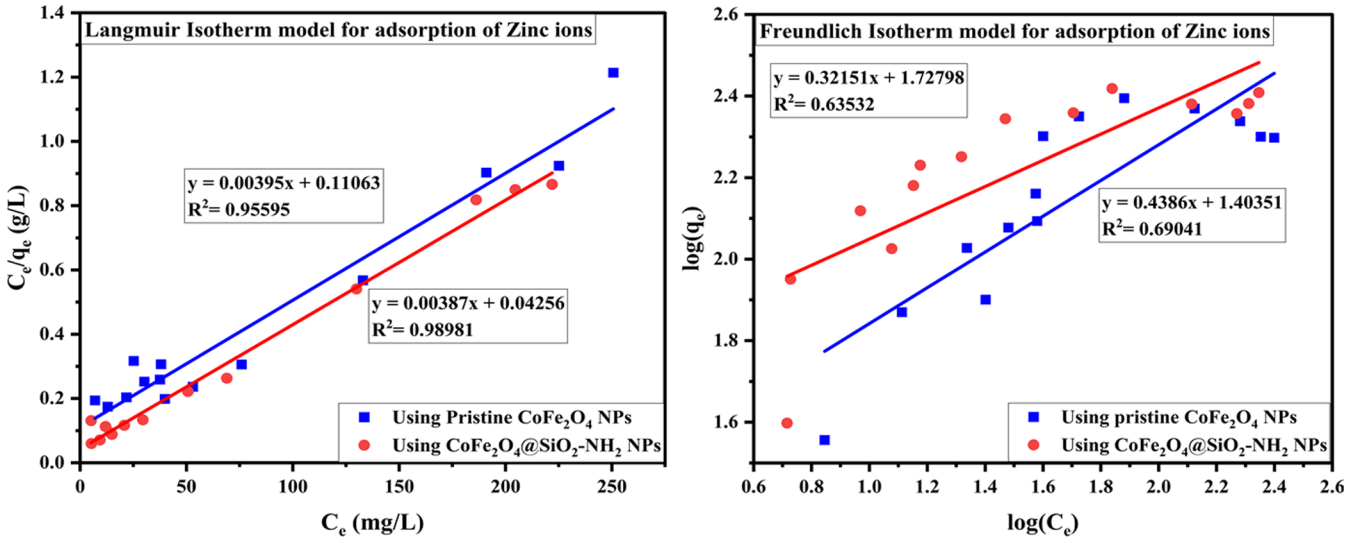

Figure 14. Isotherm models for the adsorption of Zn(II) ions.

maximal adsorption capacity based on the pseudo-second-order model is around 185.18 mg g^{-1}. According to these findings, chemisorption was involved in the adsorption of Pb(II) ions onto the functionalized adsorbent. Figure 11 displays the adsorption plots of Zn(II) ions using pseudo-first and second-order models on the pristine and functionalized adsorbents.

Adsorption Isotherms. To clearly show how the adsorbent interacts with the adsorbates, adsorption isotherms are explored using Freundlich and Langmuir isotherms. According to the Langmuir model, more binding sites on the surface of an adsorbent result in improved adsorption results. Meanwhile, the Freundlich isotherms thoroughly explain the surface adsorption of numerous adsorbents with different

https://doi.org/10.1021/acsomega.3c07200
ACS Omega 2024, 9, 3507−3524

Table 4. Comparison of the Adsorption Performance of Various Adsorbents Based on Kinetic Models

adsorbent	heavy-metal-treated	pseudo-first-order model			pseudo-second-order model			ref
		q_e (mg/g)	k_1 (1/min)	R^2	q_e (mg/g)	k_2	R^2	
$CoFe_2O_4$@SiO_2-NH_2	Cu(II)				177.8	0.000401	0.99897	49
	Pb(II)				181.6	0.000453	0.99997	
dioctylphetalate triethylenetetraamine (DOP-TETA) MNPs	Zn(II)	13.89	0.01	0.81	43.1	0.00273	0.99	62
magnetite-NH_2 NPs	Cu(II)	19.76	0.0382	0.995	24.6	0.00396	0.999	59
lemonwood biochar	Zn(II)	52.19	0.055	0.986	100	0.002	0.999	60
	Cu(II)	54.43	0.049	0.985	111.1	0.0016	0.99	
chitosan-functionalized Fe_3O_4	Pb(II)	112.4	0.03928	0.9624	152.8	0.0002	0.9613	63
Ag-FMWCNTs	Cu(II)	16.21	3.96	0.9793	16.63	6.01	0.99994	64
SPIONs/gel	Cu(II)	18.834	0.055	0.992	20.779	0.004	0.991	65
	Zn(II)	14.109	0.137	0.986	14.888	0.019	0.998	
ZnO NPs	Pb(II)	5.8	0.014	0.959	4.5	0.048	0.997	66
$CoFe_2O_4$ NPs	Cu(II)	5.364	0.00000536	0.9206	143.47	0.000486	0.9982	present work
	Pb(II)	96.49	0.0000086	0.977	151.52	0.000159	0.987	
	Zn(II)	4.788	−0.0000051	0.86	144.72	0.00063	0.999	
$CoFe_2O_4$@SiO_2-NH_2 NPs	Cu(II)	6.5986	0.0000092	0.959	180.505	0.000447	0.9986	present work
	Pb(II)	78.02	−0.000019	0.929	185.18	0.00037	0.9985	
	Zn(II)	4.96816	−0.0000081	0.929	172.12	0.00073	0.9996	

Table 5. Comparison of the Adsorption Performance of Various Adsorbents Based on Isotherm Models

adsorbent	heavy-metal-treated	Freundlich isotherm model			Langmuir isotherm model			ref
		n	K_f (mg/g)	R^2	q_{max}	K_L (L/mg)	R^2	
dioctylphetalate triethylenetetraamine (DOP-TETA) MNPs	Zn(II)	0.57	5.58	0.9	23.75	0.44	0.93	62
Fe_3O_4@SiO_2-NH_2 NPs	Zn(II)	1.6471	9.9115	0.9923	169.492	36.76	0.8094	67
chitosan-functionalized Fe_3O_4 NPs	Pb(II)	2.6716	2.369	0.9764	95.36		0.9881	63
magnetite-NH_2 NPs	Cu(II)	1.79	5.81	0.972	28.7	0.25	0.996	59
ZnO NPs	Pb(II)	2.81	3.16	0.914	19.65	0.0839	0.999	66
Ag-FMWCNTs	Cu(II)	2.71	10.58	0.9632	51.58	0.0987	0.9958	64
SPIONs/gel/PVA	Cu(II)	2.2867	45.658	0.976	56.051	3.397	0.993	65
	Zn(II)	2.2732	32.866	0.979	40.865	3.267	0.999	
chitosan-based Fe_3O_4 NCs	Cu(II)				21.5	0.0165	0.9932	68
zero-valent iron NPs	Pb(II)	3.178	19.79	0.964	124.4	0.04	0.989	69
lemonwood biochar	Zn(II)	4.41	49.77	0.91	100	0.27	0.998	60
	Cu(II)	4.06	56.1	0.975	111.1	1	0.999	
$CoFe_2O_4$ NPs	Cu(II)	0.4842	3.528	0.8319	256.41	0.0228	0.9723	present work
	Pb(II)	0.4346	3.923	0.572	210.08	0.0443	0.9355	
	Zn(II)	0.439	4.0695	0.6904	253.17	0.0357	0.956	
$CoFe_2O_4$@SiO_2-NH_2 NPs	Cu(II)	0.2491	6.665	0.796	277.008	0.1216	0.9961	present work
	Pb(II)	0.3082	5.7	0.458	254.453	0.081	0.9758	
	Zn(II)	0.3215	5.629	0.6353	258.39	0.0909	0.989	

adsorption sites.[56] Figure 12 provides a graphical representation of the adsorption of Cu(II) ions onto the adsorbent based on Langmuir and Freundlich isotherms.

Previous reports by Hao et al.[57] revealed that the $-NH_2$-functionalized nanoadsorbent exhibits maximum adsorption for Cu(II) ions. They used the Langmuir equation to determine the adsorption of approximately 25.77 mg g^{-1} at a pH of 6 and at 298 K. The resulting isotherm parameters for the pristine and functionalized adsorbent, obtained through subsequent calculations from the present study, are provided in Table 3. The maximum adsorption capacity of the adsorbent is denoted by Q_m, which is calculated from the Langmuir model using eq 12

$$Q_m = \frac{1}{\text{intercept}} \tag{12}$$

The maximal adsorption capacity is found to be around 256.41 and 277.008 mg g^{-1} for Cu(II) ions using pristine and functionalized adsorbents, respectively.

Figure 13 depicts the adsorption of Pb(II) ions onto synthesized adsorbents based on the Langmuir and Freundlich isotherm models. Calculated parameters from this study are given in Table 3. According to a study by Mahmud et al.,[58] the maximal adsorption capacity of the functionalized nanoadsorbent, as determined by the Langmuir equation, was 16.7 mg g^{-1}. The isotherm parameters were produced for both pristine and functionalized adsorbents. The maximal adsorption capacity (q_m) is calculated at around 210.08 and 254.45

https://doi.org/10.1021/acsomega.3c07200
ACS Omega 2024, 9, 3507−3524

mg g^{-1} using pristine and functionalized adsorbents, respectively. A common adsorption isotherm that explains the relationship between the concentration of the adsorbate in solution and how much of it is adsorbed onto a solid surface is called the Freundlich model. Figure 13 shows the Freundlich curve for Pb(II) adsorption onto the adsorbent. This model reveals that the adsorption procedure takes place on a surface with numerous active sites and that the adsorption increases with the adsorbate's concentration. The resulting parameters are given in Table 3. The correlation constant R^2 was considered for a better-fitted model of the adsorption of Pb(II) ions. Figure 14 shows the adsorption of Zn(II) ions using the Freundlich isotherm model and the Langmuir model. The isotherm parameters generated by utilizing both pristine and coated adsorbents are shown in Table 3. The highest adsorption (q_m) is estimated to be 253.16 and 258.39 mg g^{-1}, respectively, using pristine and coated adsorbents.

The current work demonstrates that the Langmuir and pseudo-second-order models both confirm a superior match for the adsorption of various metal ions by using both pristine and functionalized ferrites. However, functionalized adsorbents showed more adsorption efficiency than pristine adsorbents due to electrostatic attraction between oppositely charged metal ions and the amino-functionalized adsorbents. The hydroxyl (−OH) or other functional groups on the surface are very attractive to metallic ions. As observed in SEM and VSM analyses, the pristine adsorbent showed aggregation among the particles due to strong magnetic characteristics compared to modified nanoparticles.[45] The agglomeration of the particles in the pristine sample shows a small surface area available for the adsorption of metal ions. However, the size of the pristine nanoparticles was slightly smaller than that of the modified adsorbent. A small increase in size was due to the deposition of the coating material on the particle surface. The surface coating reduces the magnetic properties and prevents aggregation of the nanoparticles by offering a large reactive surface area for adsorption applications. From the Langmuir isotherm, it is inferred that the adsorption of metal ions on amino-functionalized $CoFe_2O_4@SiO_2$ is a monolayer adsorption process since the relationship between C_e/q_e and C_e shows a strong linearity. For all heavy metals, the q_m values are found to be quite comparable to the experimental values.

A comparison of the kinetic and isotherm parameters of this investigation with those in the previously published literature is summarized in Tables 4 and 5. The amino-functionalized $CoFe_2O_4@SiO_2$ outperformed the pristine $CoFe_2O_4$ adsorbent in adsorbing heavy-metal ions. The functionalized adsorbent showed a greater adsorption capacity for heavy metals than the majority of conventional adsorbents, including activated carbon, zeolites, and clay minerals. This adsorbent was also reusable, since it can be simply regenerated with a mildly acidic solution. The adsorbent was tested for a maximum of five cycles. The synthesized adsorbent showed good regeneration and stability, as reported in Figure 15. Ren et al.[49] prepared the magnetic nanoparticles using the coprecipitation method and then modified the surface using silica and amino-functionalization. The adsorbent was applied to remove heavy-metal ions from water. It showed the maximum adsorption capacity for Cu(II) and Pb(II) around 177 and 181 mg g^{-1}, respectively, at room temperature.

Li et al.[59] synthesized the amino-functionalized magnetite nanoparticles by the sol−gel method. The adsorption capacity for the removal of Cu(II) ions was achieved around 24.6 mg g^{-1} at room temperature and pH around 4. Azadian et al.[60] synthesized lemonwood-derived biochar by the biomass pyrolysis setup and modified its surface by zeolite and magnetic nanoparticles. This adsorbent showed adsorption capacities of 109.37 and 80.18 mg g^{-1} for Zn(II) and Pb(II) ions, respectively. Meng et al.[61] prepared amine-functionalized $Fe_3O_4@SiO_2$ nanoparticles using the modified Stober method to remove Fe^{3+} ions from contaminated water. The adsorbent was tested by varying the pH and contact time. This adsorbent showed maximal adsorption capacity at a pH of 2.5, which was around 20.66 mg g^{-1}. The present study revealed adsorption capacities of 277.008, 254.453, and 258.398 mg g^{-1} for Cu(II), Pb(II), and Zn(II) ions, respectively. The presented work has benefits over other adsorbents such as low cost, high adsorption capacity, and reusability.

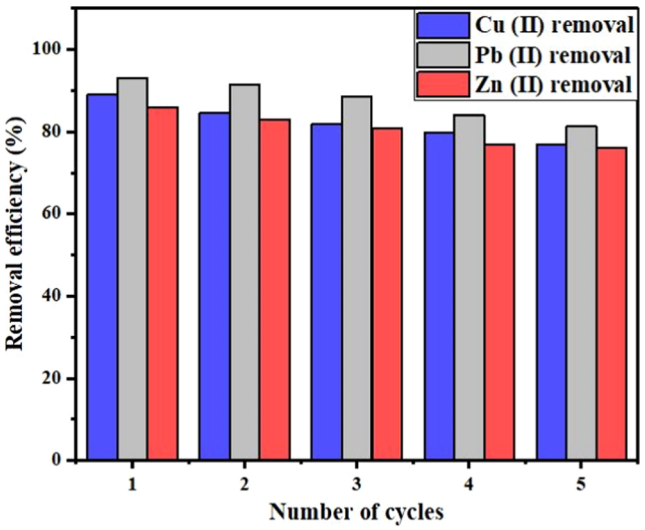

Figure 15. Efficiency of the adsorbent for Cu(II), Pb(II), and Zn(II) ions over five cycles.

Stability and Reusability Tests. The use of adsorbents in practical applications is dependent on their capacity for recycling. Data on the effectiveness of $CoFe_2O_4@SiO_2-NH_2$ in removing Cu(II), Pb(II), and Zn(II) ions during five successive recycling operations can be found in Figure 15. The initial cycle shows a Cu(II) ion adsorption removal effectiveness of about 89%. With each succeeding cycle, its efficiency, however, declines until it reaches 76% in the fifth cycle. Similar to Pb(II) and Zn(II), the first cycle shows an approximately 93 and 86% efficacy that gradually decreases to 81 and 76%, respectively, after the fifth adsorption cycle. These results show that this adsorbent has good adsorption effectiveness and can be used for a number of cycles without losing sufficient adsorption capacity.

FTIR and SEM characterization of the spent adsorbents was performed to determine their stability after multiple adsorption cycles. FTIR spectra of pristine and amino-functionalized adsorbents after five adsorption cycles are reported in Figure 16. It was observed that a slightly rough FTIR pattern was obtained after the absorption due to the attachment and deattachment of metallic ions from the surface of the adsorbent. However, there were no significant functional changes in the FTIR patterns of both pristine and functionalized adsorbents, showing high stability of the adsorbents over multiple cycles. The magnetic spinel ferrite adsorbents may undergo morphology changes during prolonged exposure to

https://doi.org/10.1021/acsomega.3c07200
ACS Omega 2024, 9, 3507−3524

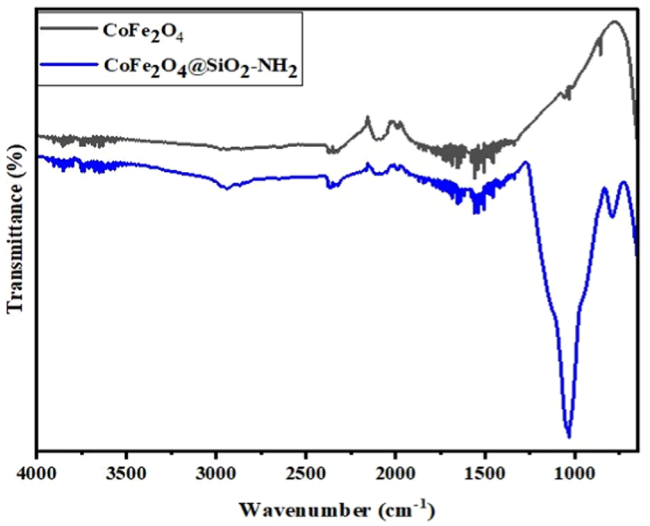

Figure 16. FTIR patterns of pristine and functionalized adsorbents after five cycles.

heavy-metal ions. The adsorption capacity of the absorbent may decrease due to the saturation of active sites on it, which results in a decrease in the removal efficiency. Therefore, SEM images of the pristine and functionalized adsorbents were taken after five cycles to check the changes in the particle size or agglomeration of the adsorbent particles. Figure 17a shows the high stability and dispersibility of the pristine adsorbent. No notable changes in surface morphology were observed before and after five adsorption cycles. However, some changes in the morphology of the functionalized adsorbent were observed at the end of the process, which slightly affected the regeneration efficiency (Figure 17b). The adsorption efficiency decreased during multiple cycles. The agglomeration of particles increased, while the particle size slightly decreased due to the removal of silica coating and the separation of functional groups during multiple adsorption cycles. It resulted in the disintegration of the larger particles, affecting the recyclability of the adsorbent.

CONCLUSIONS

This study produced $CoFe_2O_4$ ferrite nanoparticles of spherical shape through a coprecipitation approach and modified with silica, followed by amino-functionalization in a simple reaction process. The successful deposition of silica and amino groups on the magnetic adsorbent was confirmed by FTIR and UV analyses. Utilizing VSM analysis, the magnetic characteristics of the synthesized materials were evaluated. The silica and amino coatings reduced the saturation magnetization of the adsorbent. The pristine adsorbent had a saturation magnetization of 75 emu/g, which is reduced to 57 emu/g after surface modification. The functionalized adsorbent showed adsorption capacities of 277.008, 254.453, and 258.398 mg/g for Cu(II), Pb(II), and Zn(II) ions, respectively. The pseudo-second-order model correctly predicted the kinetics of the adsorption of all heavy-metal ions onto the synthesized adsorbents, pointing to a chemical adsorption mechanism. The Langmuir isotherm model, which is appropriate for the monolayer adsorption of metallic ions on the surface of the adsorbent, provided a good match with the adsorption isotherm. With an amazing removal efficiency, this adsorbent could be used at least five times with removal efficiencies of around 77, 81, and 76% for Cu(II), Pb(II), and Zn(II) ions, respectively. The amino-modified adsorbent showed higher adsorption efficiency than the pristine one due to the development of electrostatic attraction between metal ions and the oppositely charged amino-modified adsorbent. The pristine adsorbent showed more aggregation among the nanoparticles due to strong magnetic attraction compared with the amino-modified adsorbent. By providing a wide reactive surface area for adsorption applications, the amino coating decreases the magnetic characteristic and reduces the aggregation of nanoparticles. The modified adsorbent produced a large reactive surface area for interacting with adsorbate ions and, consequently, a high adsorption capacity.

ASSOCIATED CONTENT

Data Availability Statement

The available data has been included in this paper in the form of images, figures, and tables. There is no additional data to report as a separate file.

AUTHOR INFORMATION

Corresponding Authors

Shazia Shukrullah − *Department of Physics, University of Agriculture Faisalabad, 38040 Faisalabad, Pakistan;*

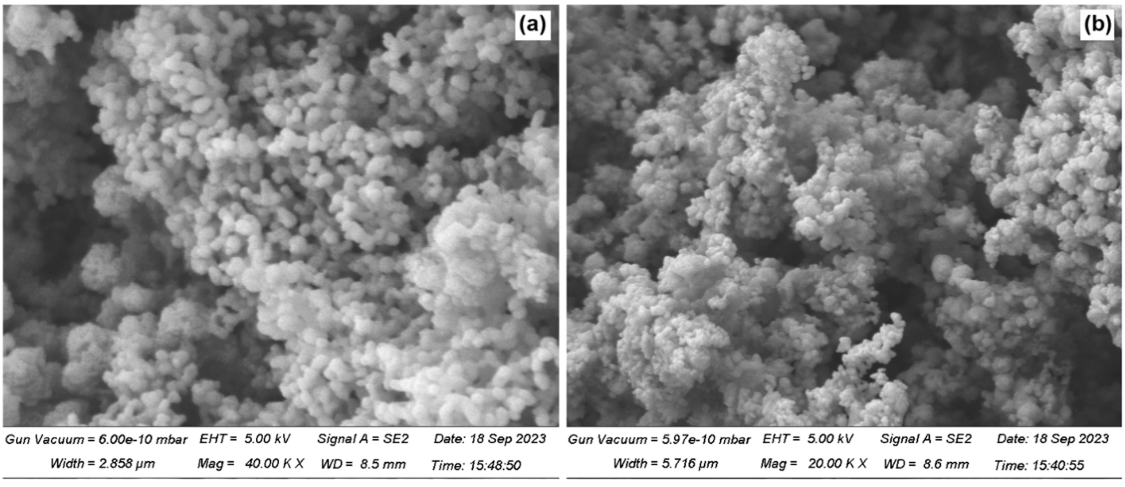

Figure 17. SEM image of (a) pristine adsorbent and (b) amino-functionalized adsorbent after five adsorption cycles.

https://doi.org/10.1021/acsomega.3c07200
ACS Omega 2024, 9, 3507−3524

orcid.org/0000-0002-4474-3768; Email: zshukrullah@gmail.com

Muhammad Yasin Naz − *Department of Physics, University of Agriculture Faisalabad, 38040 Faisalabad, Pakistan*; Email: yasin603@yahoo.com

Authors

Muhammad Umer Saleem − *Department of Physics, University of Agriculture Faisalabad, 38040 Faisalabad, Pakistan*

Humaira Hussain − *Department of Chemistry, University of Okara, 56300 Okara, Pakistan*

Muhammad Irfan − *Electrical Engineering Department, College of Engineering, Najran University Saudi Arabia, Najran 61441, Saudi Arabia*; orcid.org/0000-0003-4161-6875

Saifur Rahman − *Electrical Engineering Department, College of Engineering, Najran University Saudi Arabia, Najran 61441, Saudi Arabia*

Abdulnoor Ali Jazem Ghanim − *Civil Engineering Department, College of Engineering, Najran University, Najran 61441, Saudi Arabia*

Complete contact information is available at: https://pubs.acs.org/10.1021/acsomega.3c07200

Notes

The authors declare no competing financial interest.

■ ACKNOWLEDGMENTS

The authors acknowledge the support of this research by the Deputy for Research and Innovation Ministry of Education, the Kingdom of Saudi Arabia, through Grant Number NU/IFC/2//SERC/-/2 under the Institutional Funding Committee at the Najran University, the Kingdom of Saudi Arabia.

■ REFERENCES

(1) Liu, X.; Li, Y.; Chen, Z.; Yang, H.; Wang, S.; Tang, Z.; Wang, X. Recent Progress of COFs Membranes: Design, Synthesis and Application in Water Treatment. *Eco-Environ. Health* **2023**, *2* (3), 117−130.

(2) Fang, L.; Huang, T.; Lu, H.; Wu, X. L.; Chen, Z.; Yang, H.; Wang, S.; Tang, Z.; Li, Z.; Hu, B.; Wang, X. Biochar-Based Materials in Environmental Pollutant Elimination, H_2 Production and CO_2 Capture Applications. *Biochar* **2023**, *5* (1), No. 42.

(3) Shu, W. S.; Ye, Z. H.; Lan, C. Y.; Zhang, Z. Q.; Wong, M. H. Acidification of Lead/Zinc Mine Tailings and Its Effect on Heavy Metal Mobility. *Environ. Int.* **2001**, *26* (5−6), 389−394.

(4) Tabelin, C. B.; Igarashi, T.; Villacorte-Tabelin, M.; Park, I.; Opiso, E. M.; Ito, M.; Hiroyoshi, N. Arsenic, Selenium, Boron, Lead, Cadmium, Copper, and Zinc in Naturally Contaminated Rocks: A Review of Their Sources, Modes of Enrichment, Mechanisms of Release, and Mitigation Strategies. *Sci. Total Environ.* **2018**, *645*, 1522−1553.

(5) Izah, S. C.; Chakrabarty, N.; Srivastav, A. L. A Review on Heavy Metal Concentration in Potable Water Sources in Nigeria: Human Health Effects and Mitigating Measures. *Exposure Health* **2016**, *8*, 285−304.

(6) Singh, J.; Kalamdhad, A. S. Effects of Heavy Metals on Soil, Plants, Human Health and Aquatic Life. *Int. J. Res. Chem. Environ.* **2011**, *1* (2), 15−21.

(7) Mohod, C. V.; Dhote, J. Review of Heavy Metals in Drinking Water and Their Effect on Human Health. *Int. J. Res. Chem. Environ.* **2013**, *2* (7), 2992−2996.

(8) Ali, A. S.; US SA, A. R. Effect of Different Heavy Metal Pollution on Fish. *Res. J. Chem. Environ. Sci.* **2014**, *2* (1), 74−79.

(9) Sonone, S. S.; Jadhav, S.; Sankhla, M. S.; Kumar, R. Water Contamination by Heavy Metals and Their Toxic Effect on Aquaculture and Human Health through Food Chain. *Lett. Appl. NanoBioSci.* **2020**, *10* (2), 2148−2166.

(10) Rai, P. K.; Lee, S. S.; Zhang, M.; Tsang, Y. F.; Kim, K.-H. Heavy Metals in Food Crops: Health Risks, Fate, Mechanisms, and Management. *Environ. Int.* **2019**, *125*, 365−385.

(11) Auffan, M.; Rose, J.; Bottero, J. Y.; Lowry, G. V.; Jolivet, J. P.; Wiesner, M. R. Towards a Definition of Inorganic Nanoparticles from an Environmental, Health and Safety Perspective. *Nat. Nanotechnol.* **2009**, *4* (10), 634−641.

(12) Yao, L.; Hou, X.; Hu, S.; Wang, J.; Li, M.; Su, C.; Tade, M. O.; Shao, Z.; Liu, X. Green Synthesis of Mesoporous $ZnFe_2O_4$/C Composite Microspheres as Superior Anode Materials for Lithium-Ion Batteries. *J. Power Sources* **2014**, *258*, 305−313.

(13) Yang, J.; Hou, B.; Wang, J.; Tian, B.; Bi, J.; Wang, N.; Li, X.; Huang, X. Nanomaterials for the Removal of Heavy Metals from Wastewater. *Nanomaterials* **2019**, *9* (3), No. 424.

(14) Dave, P. N.; Chopda, L. V. Application of Iron Oxide Nanomaterials for the Removal of Heavy Metals. *J. Nanotechnol.* **2014**, *2014*, No. 398569.

(15) Lajayer, B. A.; Najafi, N.; Moghiseh, E.; Mosaferi, M.; Hadian, J. Removal of Heavy Metals (Cu^{2+} and Cd^{2+}) from Effluent Using Gamma Irradiation, Titanium Dioxide Nanoparticles and Methanol. *J. Nanostruct. Chem.* **2018**, *8*, 483−496.

(16) Afreen, S.; Talreja, N.; Chauhan, D.; Ashfaq, M. Polymer/Metal/Carbon-Based Hybrid Materials for the Detection of Heavy Metal Ions. In *Multifunctional Hybrid Nanomaterials for Sustainable Agri-Food and Ecosystems*; Elsevier, 2020; pp 335−353.

(17) de Vargas Brião, G.; de Andrade, J. R.; da Silva, M. G. C.; Vieira, M. G. A. Removal of Toxic Metals from Water Using Chitosan-Based Magnetic Adsorbents. A Review. *Environ. Chem. Lett.* **2020**, *18*, 1145−1168.

(18) Kong, X.-f.; Yang, B.; Xiong, H.; Zhou, Y.; Xue, S.; Xu, B.; Wang, S. Selective Removal of Heavy Metal Ions from Aqueous Solutions with Surface Functionalized Silica Nanoparticles by Different Functional Groups. *J. Cent. South Univ.* **2014**, *21* (9), 3575−3579.

(19) Zhao, Y.; Zhai, S.-R.; Zhai, B.; An, Q.-D. Heavy Metal Removal of Tri-Amino-Functionalized Sol−Gel Hybrids with Tailored Characteristics. *J. Sol-Gel Sci. Technol.* **2012**, *62*, 177−185.

(20) Rajendran, S.; Priya, A. K.; Kumar, P. S.; Hoang, T. K. A.; Sekar, K.; Chong, K. Y.; Khoo, K. S.; Ng, H. S.; Show, P. L. A Critical and Recent Developments on Adsorption Technique for Removal of Heavy Metals from Wastewater-A Review. *Chemosphere* **2022**, *303*, No. 135146.

(21) AbiD, B. A.; Al-Shuwaiki, N. M. Removal of Heavy Metals Using Chemicals Precipitation. *Eng.Technol. J.* **2011**, *29* (3), 595−612.

(22) Ren, C.; Ding, X.; Fu, H.; Meng, C.; Li, W.; Yang, H. Preparation of Amino-Functionalized $CoFe_2O_4$@SiO_2 Magnetic Nanocomposites for Potential Application in Absorbing Heavy Metal Ions. *RSC Adv.* **2016**, *6* (76), 72479−72486.

(23) Jayalakshmi, R.; Jeyanthi, J.; Sidhaarth, K. R. A. Versatile Application of Cobalt Ferrite Nanoparticles for the Removal of Heavy Metals and Dyes from Aqueous Solution. *Environ. Nanotechnol., Monit. Manage.* **2022**, *17*, No. 100659.

(24) Zhang, J. M.; Zhai, S. R.; Zhai, B.; An, Q. D.; Tian, G. Crucial Factors Affecting the Physicochemical Properties of Sol−Gel Produced Fe_3O_4@SiO_2−NH_2 Core−Shell Nanomaterials. *J. Sol-Gel Sci. Technol.* **2012**, *64*, 347−357.

(25) Guerrini, L.; Alvarez-Puebla, R. A.; Pazos-Perez, N. Surface Modifications of Nanoparticles for Stability in Biological Fluids. *Materials* **2018**, *11* (7), No. 1154.

(26) Ghiasi, A.; Malekpour, A. Octyl Coated Cobalt-Ferrite/Silica Core-Shell Nanoparticles for Ultrasonic Assisted-Magnetic Solid-Phase Extraction and Speciation of Trace Amount of Chromium in Water Samples. *Microchem. J.* **2020**, *154*, No. 104530.

(27) Mirzaee, S.; Shayesteh, S. F.; Mahdavifar, S. Anisotropy Investigation of Cobalt Ferrite Nanoparticles Embedded in Polyvinyl Alcohol Matrix: A Monte Carlo Study. *Polymer* **2014**, *55* (16), 3713−3719.
(28) Park, B. J.; Choi, K.-H.; Nam, K. C.; Ali, A.; Min, J. E.; Son, H.; Uhm, H. S.; Kim, H.-J.; Jung, J.-S.; Choi, E. H. Photodynamic Anticancer Activities of Multifunctional Cobalt Ferrite Nanoparticles in Various Cancer Cells. *J. Biomed. Nanotechnol.* **2015**, *11* (2), 226−235.
(29) Bohara, R. A.; Throat, N. D.; Mulla, N. A.; Pawar, S. H. Surface-Modified Cobalt Ferrite Nanoparticles for Rapid Capture, Detection, and Removal of Pathogens: A Potential Material for Water Purification. *Appl. Biochem. Biotechnol.* **2017**, *182*, 598−608.
(30) Viltužnik, B.; Košak, A.; Zub, Y. L.; Lobnik, A. Removal of Pb(II) Ions from Aqueous Systems Using Thiol-Functionalized Cobalt-Ferrite Magnetic Nanoparticles. *J. Sol-Gel Sci. Technol.* **2013**, *68*, 365−373.
(31) Houshiar, M.; Zebhi, F.; Razi, Z. J.; Alidoust, A.; Askari, Z. Synthesis of Cobalt Ferrite ($CoFe_2O_4$) Nanoparticles Using Combustion, Coprecipitation, and Precipitation Methods: A Comparison Study of Size, Structural, and Magnetic Properties. *J. Magn. Magn. Mater.* **2014**, *371*, 43−48.
(32) Aygar, G.; Kaya, M.; Özkan, N.; Kocabıyık, S.; Volkan, M. Preparation of Silica Coated Cobalt Ferrite Magnetic Nanoparticles for the Purification of Histidine-Tagged Proteins. *J. Phys. Chem. Solids* **2015**, *87*, 64−71.
(33) Wang, X.; Zhang, Z.; Zhao, Y.; Xia, K.; Guo, Y.; Qu, Z.; Bai, R. A Mild and Facile Synthesis of Amino Functionalized $CoFe_2O_4$@SiO_2 for Hg (II) Removal. *Nanomaterials* **2018**, *8* (9), No. 673.
(34) Lan, S.; Wu, X.; Li, L.; Li, M.; Guo, F.; Gan, S. Synthesis and Characterization of Hyaluronic Acid-Supported Magnetic Microspheres for Copper Ions Removal. *Colloids Surf., A* **2013**, *425*, 42−50.
(35) Zhang, Y.; Yang, Z.; Yin, D.; Liu, Y.; Fei, C.; Xiong, R.; Shi, J.; Yan, G. Composition and Magnetic Properties of Cobalt Ferrite Nano-Particles Prepared by the Co-Precipitation Method. *J. Magn. Magn. Mater.* **2010**, *322* (21), 3470−3475.
(36) Zalite, I.; Heidemane, G.; Grabis, J.; Maiorov, M. The Synthesis and Characterization of Nickel and Cobalt Ferrite Nanopowders Obtained by Different Methods. In *Powder Technology*; Alberto Adriano Cavalheiro, 2018.
(37) Zhang, R.; Sun, L.; Wang, Z.; Hao, W.; Cao, E.; Zhang, Y. Dielectric and Magnetic Properties of $CoFe_2O_4$ Prepared by Sol-Gel Auto-Combustion Method. *Mater. Res. Bull.* **2018**, *98*, 133−138.
(38) Xia, K.; Guo, Y.; Shao, Q.; Zan, Q.; Bai, R. Removal of Mercury (II) by EDTA-Functionalized Magnetic CoFe2O4@SiO2 Nanomaterial with Core-Shell Structure. *Nanomaterials* **2019**, *9* (11), No. 1532.
(39) Akhtar, K.; Javed, Y.; Jamil, Y.; Muhammad, F. Functionalized Cobalt Ferrite Cubes: Toxicity, Interactions and Mineralization into Ferritin Proteins. *Appl. Nanosci.* **2020**, *10*, 3659−3674.
(40) Barde, N. P.; Shewale, S. S.; Solanki, P. S.; Shah, N. A.; Bardapurkar, P. P. Effect of Silica Matrix on Structural, Optical and Electrical Properties of $Li_{0.5}Fe_{2.5}O_4$ Nanoparticles. *Scr. Mater.* **2021**, *194*, No. 113712.
(41) Kulshrestha, R.; Anand, V. Synthesis and Characterization of Pure Cobalt Ferrite for DC Electrical. *Int. J. Innovative Technol. Explor. Eng.* **2019**, *8*, 203−207.
(42) Erdem, D.; Bingham, N. S.; Heiligtag, F. J.; Pilet, N.; Warnicke, P.; Heyderman, L. J.; Niederberger, M. $CoFe_2O_4$ and $CoFe_2O_4$-SiO_2 Nanoparticle Thin Films with Perpendicular Magnetic Anisotropy for Magnetic and Magneto-Optical Applications. *Adv. Funct. Mater.* **2016**, *26* (12), 1954−1963.
(43) Bardapurkar, P. P.; Dalvi, S. N.; Joshi, V. D.; Solanki, P. S.; Rathod, V. R.; Shah, N. A.; Barde, N. P. Effect of Silica Matrix on Structural and Optical Properties of Cobalt Ferrite Nanoparticles. *Results Surf. Interfaces* **2022**, *8*, No. 100081.
(44) Rohilla, S.; Kumar, S.; Aghamkar, P.; Sunder, S.; Agarwal, A. Investigations on Structural and Magnetic Properties of Cobalt Ferrite/Silica Nanocomposites Prepared by the Coprecipitation Method. *J. Magn. Magn. Mater.* **2011**, *323* (7), 897−902.
(45) Ristic, M.; Krehula, S.; Reissner, M.; Jean, M.; Hannoyer, B.; Musić, S. Synthesis and Properties of Precipitated Cobalt Ferrite Nanoparticles. *J. Mol. Struct.* **2017**, *1140*, 32−38.
(46) Yang, X.; Wu, W.; Xie, Y.; Hao, M.; Liu, X.; Chen, Z.; Yang, H.; Waterhouse, G. I. N.; Ma, S.; Wang, X. Modulating Anion Nanotraps via Halogenation for High-Efficiency $^{99}TcO_4^-$/ReO_4−Removal under Wide-Ranging PH Conditions. *Environ. Sci. Technol.* **2023**, *57* (29), 10870−10881.
(47) Liu, X.; Xie, Y.; Li, Y.; Hao, M.; Chen, Z.; Yang, H.; Waterhouse, G. I. N.; Ma, S.; Wang, X. Functional Carbon Capsules Supporting Ruthenium Nanoclusters for Efficient Electrocatalytic $^{99}TcO_4$−/ReO_4^- Removal from Acidic and Alkaline Nuclear Wastes. *Adv. Sci.* **2023**, No. 2303536.
(48) Zhang, J.; Zhai, S.; Li, S.; Xiao, Z.; Song, Y.; An, Q.; Tian, G. Pb(II) Removal of Fe_3O_4@ SiO_2−NH_2 Core−Shell Nanomaterials Prepared via a Controllable Sol−Gel Process. *Chem. Eng. J.* **2013**, *215*, 461−471.
(49) Ren, C.; Ding, X.; Fu, H.; Li, W.; Wu, H.; Yang, H. Core−Shell Superparamagnetic Monodisperse Nanospheres Based on Amino-Functionalized $CoFe_2O_4$@SiO_2 for Removal of Heavy Metals from Aqueous Solutions. *RSC Adv.* **2017**, *7* (12), 6911−6921.
(50) Un, U. T.; Ocal, S. E. Removal of Heavy Metals (Cd, Cu, Ni) by Electrocoagulation. *Int. J. Environ. Sci. Dev.* **2015**, *6* (6), 425−429.
(51) Kocaoba, S.; Orhan, Y.; Akyüz, T. Kinetics and Equilibrium Studies of Heavy Metal Ions Removalby Use of Natural Zeolite. *Desalination* **2007**, *214* (1−3), 1−10.
(52) Kandasamy, S.; Velusamy, S.; Thirumoorthy, P.; Periyasamy, M.; Gopalakrishnan, K. M.; Sathish, U.; Kiramani, V.; Antrini, F. D. G.; Periyasamy, S. Adsorption of Chromium Ions from Aqueous Solutions by Synthesized Nanoparticles. *J. Nanomater.* **2022**, *2022*, No. 6214438.
(53) Vamvakidis, K.; Kostitsi, T. M.; Makridis, A.; Dendrinou-Samara, C. Diverse Surface Chemistry of Cobalt Ferrite Nanoparticles to Optimize Copper(Ii) Removal from Aqueous Media. *Materials* **2020**, *13* (7), No. 1537.
(54) Sahare, S. P.; Wankhade, A. V.; Sinha, A. K.; Zodape, S. P. Modified Cobalt Ferrite Entrapped Chitosan Beads as a Magnetic Adsorbent for Effective Removal of Malachite Green and Copper (II) Ions from Aqueous Solutions. *J. Inorg. Organomet. Polym. Mater.* **2023**, *33* (1), 266−286.
(55) Baghaei, P. A. M.; Mogaddam, M. R. A.; Farajzadeh, M. A.; Mohebbi, A.; Sorouraddin, S. M. Application of Deep Eutectic Solvent Functionalized Cobalt Ferrite Nanoparticles in Dispersive Micro Solid Phase Extraction of Some Heavy Metals from Aqueous Samples Prior to ICP-OES. *J. Food Compos. Anal.* **2023**, *117*, No. 105125.
(56) Irfan, M.; Zaheer, F.; Hussain, H.; Naz, M. Y.; Shukrullah, S.; Legutko, S.; Mahnashi, M. H.; Alsaiari, M. A.; Ghanim, A. A. J.; Rahman, S.; Alshorman, O.; Alkahtani, F. S.; Khan, M. K. A.; Kruszelnicka, I.; Ginter-Kramarczyk, D. Kinetics and Adsorption Isotherms of Amine-Functionalized Magnesium Ferrite Produced Using Sol-Gel Method for Treatment of Heavy Metals in Wastewater. *Materials* **2022**, *15* (11), No. 4009.
(57) Hao, Y. M.; Man, C.; Hu, Z. B. Effective Removal of Cu(II) Ions from Aqueous Solution by Amino-Functionalized Magnetic Nanoparticles. *J. Hazard. Mater.* **2010**, *184* (1−3), 392−399.
(58) Mahmud, M.; Hossain, M. S.; Mobarak, M. B.; Sultana, S.; Sharmin, S.; Ahmed, S. Co-Precipitation Synthesis of Non-Cytotoxic and Magnetic Cobalt Ferrite Nanoparticles for Purging Heavy Metal from the Aqueous Medium: Pb(II) Adsorption Isotherms and Kinetics Study. *Chem. Ecol.* **2022**, *38* (6), 544−563.
(59) Li, H.; Xiao, D.-l.; He, H.; Lin, R.; Zuo, P.-l. Adsorption Behavior and Adsorption Mechanism of Cu(II) Ions on Amino-Functionalized Magnetic Nanoparticles. *Trans. Nonferrous Met. Soc. China* **2013**, *23* (9), 2657−2665.

https://doi.org/10.1021/acsomega.3c07200
ACS Omega 2024, 9, 3507−3524

(60) Azadian, M.; Gilani, H. G. Adsorption of Cu^{2+}, Cd^{2+}, and Zn^{2+} by Engineered Biochar: Preparation, Characterization, and Adsorption Properties. *Environ. Prog. Sustainable Energy* **2023**, No. e14088.
(61) Meng, C.; Zhikun, W.; Qiang, L.; Chunling, L.; Shuangqing, S.; Songqing, H. Preparation of Amino-Functionalized Fe_3O_4@ $MSiO_2$ Core-Shell Magnetic Nanoparticles and Their Application for Aqueous Fe3+ Removal. *J. Hazard. Mater.* **2018**, *341*, 198−206.
(62) Ghasemi, N.; Ghasemi, M.; Moazeni, S.; Ghasemi, P.; Alharbi, N. S.; Gupta, V. K.; Agarwal, S.; Burakova, I. V.; Tkachev, A. G. Zn(II) Removal by Amino-Functionalized Magnetic Nanoparticles: Kinetics, Isotherm, and Thermodynamic Aspects of Adsorption. *J. Ind. Eng. Chem.* **2018**, *62*, 302−310.
(63) Christopher, F. C.; Anbalagan, S.; Kumar, P. S.; Pannerselvam, S. R.; Vaidyanathan, V. K. Surface Adsorption of Poisonous Pb(II) Ions from Water Using Chitosan Functionalised Magnetic Nanoparticles. *IET Nanobiotechnol.* **2017**, *11* (4), 433−442.
(64) Ramana, D. V.; Yu, J. S.; Seshaiah, K. Silver Nanoparticles Deposited Multiwalled Carbon Nanotubes for Removal of Cu(II) and Cd (II) from Water: Surface, Kinetic, Equilibrium, and Thermal Adsorption Properties. *Chem. Eng. J.* **2013**, *223*, 806−815.
(65) Dolgormaa, A.; Lv, C.; Li, Y.; Yang, J.; Yang, J.; Chen, P.; Wang, H.; Huang, J. Adsorption of Cu(II) and Zn(II) Ions from Aqueous Solution by Gel/PVA-Modified Super-Paramagnetic Iron Oxide Nanoparticles. *Molecules* **2018**, *23* (11), No. 2982.
(66) Azizi, S.; Shahri, M. M.; Mohamad, R. Green Synthesis of Zinc Oxide Nanoparticles for Enhanced Adsorption of Lead Ions from Aqueous Solutions: Equilibrium, Kinetic and Thermodynamic Studies. *Molecules* **2017**, *22* (6), No. 831.
(67) Bao, S.; Tang, L.; Li, K.; Ning, P.; Peng, J.; Guo, H.; Zhu, T.; Liu, Y. Highly Selective Removal of Zn(II) Ion from Hot-Dip Galvanizing Pickling Waste with Amino-Functionalized Fe_3O_4@ SiO_2 Magnetic Nano-Adsorbent. *J. Colloid Interface Sci.* **2016**, *462*, 235−242.
(68) Chang, Y. C.; Chen, D. H. Preparation and Adsorption Properties of Monodisperse Chitosan-Bound Fe_3O_4 Magnetic Nanoparticles for Removal of Cu(II) Ions. *J. Colloid Interface Sci.* **2005**, *283* (2), 446−451.
(69) Sepehri, S.; Kanani, E.; Abdoli, S.; Rajput, V. D.; Minkina, T.; Lajayer, B. A. Pb(II) Removal from Aqueous Solutions by Adsorption on Stabilized Zero-Valent Iron Nanoparticles—a Green Approach. *Water* **2023**, *15* (2), No. 222.

https://doi.org/10.1021/acsomega.3c07200
ACS Omega 2024, 9, 3507−3524